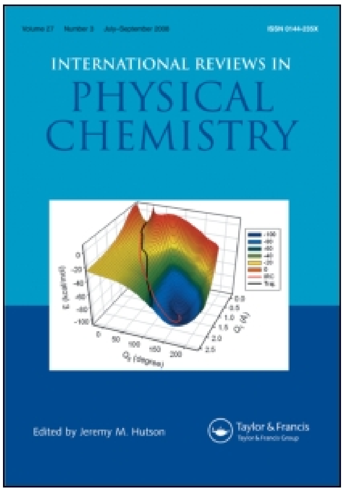

International Reviews in Physical Chemistry
Publication details, including instructions for authors and subscription information:
http://www.informaworld.com/smpp/title~content=t713724383

Vapor-deposited water and nitric acid ices: Physical and chemical properties

Ming-Taun Leu[a]; Leon F. Keyser[a]
[a] Science Division, Jet Propulsion Laboratory, California Institute of Technology, Pasadena, CA 91109, USA

To cite this Article Leu, Ming-Taun and Keyser, Leon F.(2009) 'Vapor-deposited water and nitric acid ices: Physical and chemical properties', International Reviews in Physical Chemistry, 28: 1, 53 — 109

To link to this Article: DOI: 10.1080/01442350802617129

URL: http://dx.doi.org/10.1080/01442350802617129

International Reviews in Physical Chemistry
Vol. 28, No. 1, January–March 2009, 53–109

Vapor-deposited water and nitric acid ices: Physical and chemical properties

Ming-Taun Leu* and Leon F. Keyser

Science Division, Jet Propulsion Laboratory, California Institute of Technology, Pasadena, CA 91109, USA

(*Received 1 October 2008; final version received 11 November 2008*)

Ices formed by vapor deposition have been the subject of numerous laboratory investigations in connection with snow and glaciers on the ground, ice clouds in the terrestrial atmosphere, surfaces of other planets and their satellites, and the interstellar medium. In this review we will focus on these specific subjects: (1) heterogeneous chemistry on the surfaces of polar stratospheric clouds (PSCs) and (2) surfaces of satellites of the outer planets in our solar system. Stratospheric ozone provides a protective shield for mankind and the global biosphere from harmful ultraviolet solar radiation. In past decades, theoretical atmospheric models for the calculation of ozone balance frequently used only homogeneous gas–phase reactions in their studies. Since the discovery of the Antarctic ozone hole in 1985, however, it has been demonstrated that knowledge of heterogeneous reactions on the surface of PSCs is definitely needed to understand this significant natural event due to the anthropogenic emission of chlorofluorocarbons (CFCs). We will briefly discuss the experimental techniques for the investigation of heterogeneous chemistry on ice surfaces carried out in our laboratories. The experimental apparatus used include: several flow-tube reactors, an electron-impact ionization mass spectrometer, a Fourier transform infrared spectrometer, a BET adsorption apparatus, and a scanning environmental electron microscope. The adsorption experiments and electron microscopic work have demonstrated that the vapor-deposited ices are highly porous. Therefore, it is necessary to develop theoretical models for the elucidation of the uptake and reactivity of trace gases in porous ice substrates. Several measurements of uptake and reaction probabilities of these trace gases on water ices and nitric acid ices have been performed under ambient conditions in the upper troposphere and lower stratosphere, mainly in the temperature range 180–220 K. The trace gases of atmospheric importance in heterogeneous chemistry include: $ClONO_2$, HCl, HOCl, and HNO_3. In addition, recent interest in the possible landing of a robotic spacecraft on the surface of Europa, one of the Galilean satellites of Jupiter, and ground based telescopic observations demand detailed knowledge of the physical properties of the icy surfaces of the outer planets and their satellites. Lower temperature studies in the range 77–150 K using both electron microscopy and adsorption isotherms (BET surface area measurements) have revealed some intriguing observations that may provide some insights for remote sensing of these satellite surfaces. Finally, we will attempt to summarize our recent results and suggest future research directions in both theoretical and laboratory investigations.

---

*Corresponding author. Email: Ming–Taun.Leu@jpl.nasa.gov

ISSN 0144–235X print/ISSN 1366–591X online

DOI: 10.1080/01442350802617129
http://www.informaworld.com

Keywords: water ice; nitric acid ice; vapor deposition; physical and chemical properties; heterogeneous reactions; satellite surface

Contents

1. Introduction

Water ice has been observed to be an important constituent in the solar system. Ice covers large areas of the Earth's surface, including lake and ocean ice, snow, glacier, and polar ice. In winter, ice crystals are frequently formed in clouds from the upper troposphere to the lower stratosphere and mesosphere. The Martian polar cap, comets, satellite surfaces of the outer planets in the solar system, and the interstellar medium are also known to comprise water ice.

Water ice can be formed by either freezing from the liquid or by deposition from the vapor [1]. The physical properties including phase, granular size, and morphology are significantly different depending upon the formation mechanisms. In this review we will focus on the physical and chemical properties of vapor–deposited ice only. Growth of ice from the vapor phase has been used to investigate granular sizes, phases, morphologies, physical adsorption, and chemical reactivity in laboratories around the world. It is well known that amorphous ice forms below $\sim$150 K, cubic ice between $\sim$150 K and $\sim$200 K, and hexagonal ice above $\sim$200 K [1]. Two comprehensive treatments of ice physics have been widely cited in the literature [1,2]. In this review we will focus on the physical and chemical properties important in the laboratory investigations of heterogeneous chemistry in the Antarctic stratosphere and satellite surfaces of the outer planets in the solar system. These studies were carried out at the NASA–Jet Propulsion Laboratory.

1.1. *Gas-ice interactions*

Gas-ice crystal interactions involve a number of transport and chemical conversion processes. These processes include gas diffusion, mass accommodation and evaporation to and from the interface, solid ice diffusion, solubility, and chemical reaction. Gas phase diffusion is now well established and characteristic diffusion coefficients in air or helium have been measured or can be easily calculated [3]. On the other hand, since solid phase diffusion is very slow, gas-ice interactions can be considered as a first approximation to occur only on the surfaces of ice granules. In Section 4, we will discuss in greater detail the theory of surface reaction and diffusion in porous ices. Typically, the rate coefficient used to represent an uptake (or mass accommodation) process or a chemical reaction can be defined as γ (or α), where

$$\gamma = \frac{\text{Number of gas molecules removed by reaction or uptake on the ice surface}}{\text{Number of gas molecules colliding with the ice surface}} \tag{1}$$

By definition, γ must be less than unity. Since the surface area of ice crystals in the atmosphere is rather low, relatively high γ values are required for the process to play an important role in atmospheric chemistry.

1.2. *Heterogeneous reactions in the Antarctic stratosphere*

Historically, gas–phase reactions were the major focus of laboratory studies of atmospheric processes until the discovery of the Antarctic ozone hole in 1985 [4]. The large increase in ozone depletion and high concentrations of chlorine monoxide (ClO) cannot be explained by these homogeneous gas–phase reactions alone. Several heterogeneous reactions on the surface of polar stratospheric clouds (PSCs) have been proposed, for example

$$\mathrm{ClONO_2(g) + HCl(a) \rightarrow Cl_2(g) + HNO_3(a)} \tag{2}$$

$$\mathrm{ClONO_2(g) + H_2O(a) \rightarrow HOCl(g) + HNO_3(a)} \tag{3}$$

$$\mathrm{HOCl(g) + HCl(a) \rightarrow Cl_2(g) + H_2O(a)} \tag{4}$$

In Equation (2)–(4), (g) refers to a species in the gas phase and (a) refers to a species adsorbed on the solid ice surface. The rate coefficients of these reactions have been subsequently measured in the laboratory [5,6] and these results have been successfully used in theoretical models to explain the observed high ClO concentrations [7]. These suggested reactions have been proved beyond any reasonable doubt to be responsible for the huge loss of atmospheric ozone through the powerful catalytic ClO–ClO reaction chain [8] and other catalytic reaction mechanisms during springtime in the Antarctic stratosphere [9].

PSCs are thought to consist of two types:

- Type I are formed at ambient temperatures between 185 and 200 K, and consist of submicron- or micron-sized aerosols containing (a) solid crystals of nitric acid trihydrate, (b) nitric acid dihydrate, and (c) a ternary solution of $HNO_3/H_2SO_4/H_2O$ [10].
- Type II are observed at colder temperatures, below 185 K, and consist of large water ice crystals 10–100 μm in diameter [11].

The concentration of Type I PSCs is much higher than that of Type II in the springtime Antarctic stratosphere.

1.3. *Surfaces of the satellites of the outer planets*

Most satellites in the outer solar system have surfaces substantially covered by water ice. Near-infrared reflection spectra of Jupiter's icy satellites collected by the Galileo spacecraft Near-Infrared Mapping Spectrometer (NIMS) instrument fit well with ice models using single or closely spaced bimodal grain sizes in the range from 10 to several 100 μm; the degree of closeness of the fits varies with the satellite and the location where near–infrared reflection spectra were taken on a particular satellite [12,13]. Moreover, Hansen *et al.* [14,15] also investigated reflection spectra of Saturn's icy moons from the Cassini Visual and Infrared Mapping Spectrometer (VIMS) instrument and deduced that grain sizes ranging from 1–5 μm are a good fit to the ice models. The inferred ice grain sizes are consistent with the differential temperatures between Galilean and Saturnian satellites. These results motivated us to investigate ice granule sizes using electron microscopy.

The phase curves derived from observations of the icy Galilean satellites have been used to analyze surface structure [16]. These models used Hapke's theory to analyze the 0.47 and 0.55 μm bands from Earth–based telescopic observations and from the Voyager mission. Buratti [17,18] concluded that the surfaces of Ganymede and Callisto consist of 80% and 90% of void space, respectively. Domingue and colleagues [19,20] observed that Europa has a much brighter surface than the other satellites, and therefore consists of ~96% of void space. These theoretical results provided a motivation for us to investigate ice porosities by a photometric method at lower temperatures (77–150 K) [21].

1.4. *Scope of present review*

In the sections that follow, we first discuss the experimental methods used to measure reaction probabilities, sticking coefficients and uptake efficiencies. Next we present morphological and optical studies of the ice substrates, including electron microscopy, surface area measurements, ice porosity, and infrared spectrometry. Next, theoretical models based on these morphology results are discussed generally and then in a more simplified layer interpretation. Next the results of uptake and reactivity measurements are presented; some of these results are discussed in terms of the theoretical models. The theory is also applied to some solid powder substrates. Finally we summarize our work and discuss possible future directions for this research.

2. Reactivity and uptake measurements

In this section we discuss the experimental methods used (1) to determine reaction probabilities and sticking coefficients, and (2) to carry out uptake measurements of HCl. We have used several types of fast flow-tube reactors for these measurements. Details will be given in the following sections.

2.1. *Reaction probability and sticking coefficient measurements*

The flow reactor was made of borosilicate glass, typically 60 cm in length and 2.5 cm inside diameter as shown in Figure 1 [22]. Ice films were prepared on the inner wall of the reactor by vapor deposition. Deposition temperature was regulated by circulating cold methanol

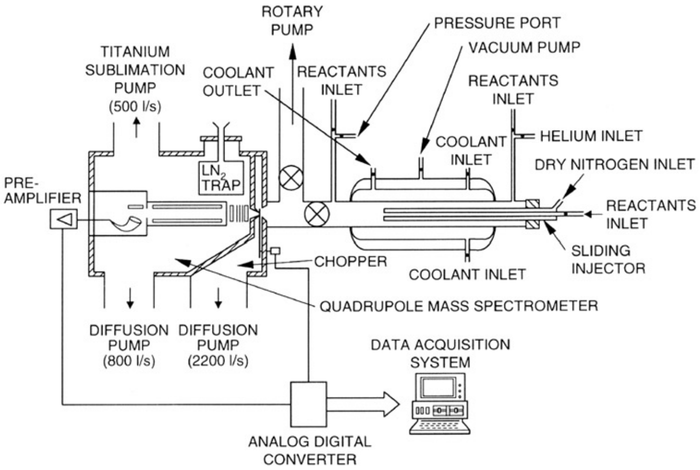

Figure 1. Schematic diagram of the flow-tube reactor coupled to an electron–impact ionization mass spectrometer.

through the outside jacket surrounding the flow reactor and measured by a thermocouple attached to the middle section. The pressure inside the reactor was monitored by a high–precision capacitance manometer which was located a few cm from the reactor at the downstream end. The measured pressure was corrected for the viscous pressure gradient between the measurement point and the midpoint of the reactor. The reactants, such as HCl or $ClONO_2$, were added through a sliding borosilicate injector as shown in Figure 1. The carrier gas was helium in the ice-coated reactor. The average flow velocity in the neutral flow reactor was between 300 and 3000 cm s^{-1}. A large valve located at the downstream end of the neutral reactor was used to regulate the flow velocity.

The reaction probabilities were determined as follows. The loss rates of reactants, k_s(obs), were measured as a function of injector position, z, according to the following equation

$$k_s(\mathrm{obs}) = -v\mathrm{d}\ln[C]/\mathrm{d}z \tag{5}$$

where C is the reactant concentration and v is the average flow velocity. The reaction time was calculated by using $t = z/v$. In each experiment we calculated the cross-sectional area of the reactor and then the flow velocity. The first-order rate constant, k_s(obs), was calculated from the slope of a linear least-squares fit to the experimental data. Using the data analysis procedures reported by Brown [23], we made the axial and radial gas-phase diffusion corrections to k_s(obs). The rate corrected for gas-phase diffusion was designated as k_g. The above-mentioned treatment has been applied to the laboratory studies using the coated reactor.

The reaction probability or uptake coefficient for the coated reactor was calculated from the k value by using the following equation [24–26]

$$\gamma = 2r_o k/(\omega + r_o k) \tag{6}$$

where r_o is the radius of the flow rector and ω is the mean molecular velocity of the reactant. Reaction probability and sticking coefficient measurements are based on the geometric area of the reactor. Corrections for the internal porosity and external roughness of ice substrates using either an analytical model or a layer model will be discussed in Section 4. The final results for several important atmospheric reactions will be presented in Section 5.

2.2. *Uptake measurements*

The uptake of HCl in water ice was investigated in a U–shaped flow reactor interfaced with a mass spectrometer [22,27]. Ice substrates were prepared on the inner wall of the reactor by vapor deposition. The thickness or mass of ices was controlled by the deposition rates and flow rates. The reactor was cooled in a methanol/dry ice reservoir. HCl–He mixtures were prepared in a glass manifold which was previously evacuated to less than 10^{-6} torr. At first the HCl–He mixture was admitted to the flow reactor through an inlet located at the downstream end; this bypassed the ice film and allowed the vacuum lines to be conditioned with HCl. At the start of a typical experiment, the flow was redirected through another inlet at the upstream end of the ice film. The uptake was measured by integrating the signals over the reaction time. Results on the uptake of HCl will be discussed in Section 5.3.

3. Morphological and optical studies of ice substrates

To understand the structures of water ice and nitric acid ice substrates coated on the inner walls of flow-tube reactors, we have used electron microscopy, BET adsorption isotherms, porosity measurements and infrared spectrometry. The experimental details and results of these characterizations will be discussed below.

3.1. *Environmental scanning electron microscopy (ESEM)*

The recent development of high-pressure and high-humidity electron microscopy has been very valuable in the investigation of granule size, shape and packing of ices. Details of our studies are given as follows.

3.1.1. *Experimental details of studies using ESEM*

By using the ESEM technique, we were able to form and study ice films under conditions (temperature, pressure, deposition rate, sample size, film thickness, and substrate) similar to those used in the uptake and reaction probability measurements. A schematic of the ESEM setup is illustrated in Figure 2. The films were deposited by condensing H_2O vapor or a mixture of HNO_3 and H_2O vapors onto cold borosilicate, aluminum or silicon substrates mounted on a cold stage within the specimen chamber of an ESEM instrument. During the cool down period, the chamber was either evacuated or purged with a stream of dry nitrogen. When the substrate was at the desired deposition temperature (usually below about 200 K), H_2O or H_2O and HNO_3 vapors in a stream of nitrogen or air were passed into the chamber through a micro-injector directed approximately parallel and positioned so that its tip was about 2.5 cm from the substrate surface.

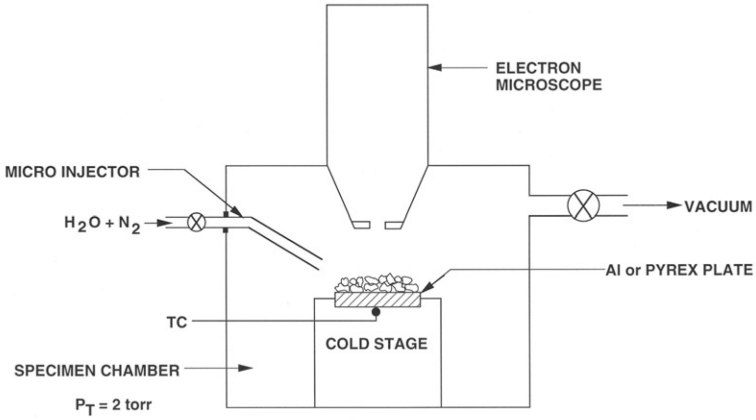

Figure 2. Schematic diagram of the configuration of the environmental scanning electron microscope.

To obtain HNO_3–H_2O ice films near the composition of $HNO_3 \cdot 3H_2O$ (NAT), the vapors were sampled over a 63 wt% HNO_3 solution; at 20°C the ratio of H_2O and HNO_3 vapors is about 3/1. Earlier work has shown that films prepared in this way have overall compositions near that of the trihydrate ($HNO_3 \cdot 3H_2O$). For pure H_2O ice films the vapor was obtained from a liquid reservoir near 20°C. Reagent grade HNO_3 and distilled or deionized H_2O were used. Deposition temperatures were between 77 and 273 K; total chamber pressure was between 2 and 3.5 torr with H_2O and HNO_3 partial pressures around 0.04 torr. Film thicknesses were 10–50 μm. In a few cases a micro-manipulator was used to remove some of the ice granules situated at the top of the ice film so that internal packing structures and porosities of these films could be observed directly. The silicon plate was extremely smooth; surface irregularities such as cracks or pits were smaller than 0.1 μm, the highest resolution at which the microscope was operated. However, the surfaces of the aluminum and borosilicate plates were found to have hairline cracks and machine tool marks. The smoothness of these plates affects the size of the granules comprising the ice films as will be discussed below. Additional experimental details have been presented earlier [28].

3.1.2. *Structures of ice films revealed by electron microscopy*

3.1.2.1. *Film growth (200–220 K)*. Film growth was observed during deposition near 200 K for both H_2O and NAT ices. Typical micrographs for borosilicate substrates are given in Figures 3 and 4 and show that the films are comprised of granules of roughly uniform size, with a few larger agglomerates. The very earliest stages of condensation were difficult to record; but after several minutes, individual granules were clearly observable. The granules increased in size with deposition time and, hence, with thickness. Granule sizes ranged from about 1 to 8 μm for deposition times up to 20 minutes or more. From micrographs (Figure 5a) taken near the substrate edge, we estimate that the films were less than about 20 μm thick at the end of the deposition. Water ice sometimes formed cubic granules as shown in Figure 3(a) and Figure 3(b); sizes ranged from about 1 to 5 μm

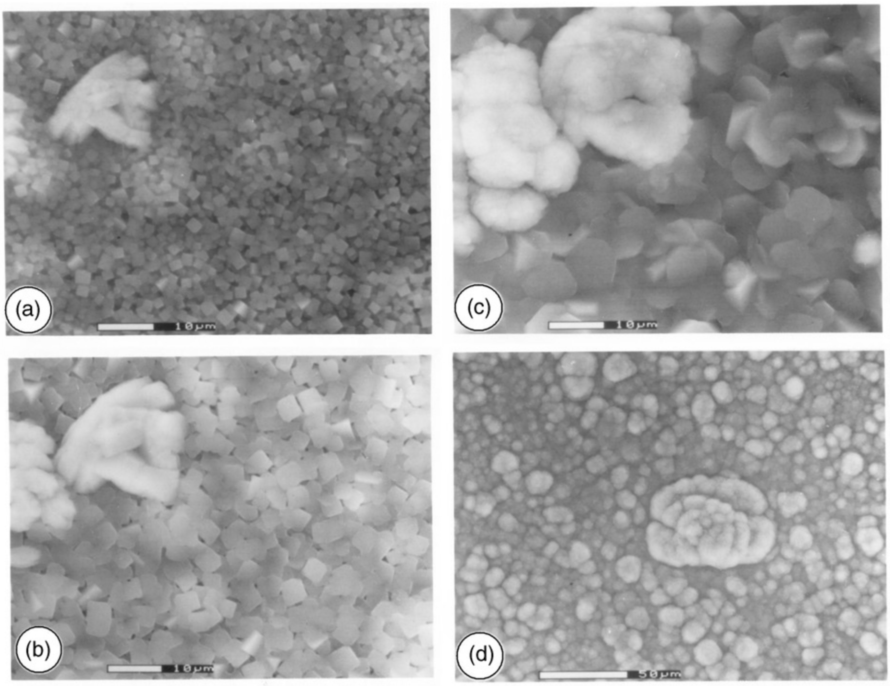

Figure 3. The figure is taken from Figure 2 of Keyser and Leu [28]. Electron micrographs of an H_2O ice film formed by vapor deposition onto a borosilicate substrate. Panels a–c show film growth during the deposition process at 200–202 K. Panel d shows effect of warming the film to 220 K. Total observation times since the start of deposition are 20 min (a), 22 min (b), 26 min (c) and 35 min (d).

during the observation time. The cubic phase is metastable at these temperatures and rapidly converts to the hexagonal form as shown in Figure 3(c). During some experiments the cubic phase did not form and only hexagonal or irregularly shaped granules were observed from the start of the deposition. When the ice films were warmed above the deposition temperature, the granules increased slowly in size and some sintering was observed (see Figures 3d and 4d). Results using aluminum substrates are very similar.

3.1.2.2. *Effect of annealing (180–230 K).* The effect of annealing was investigated in detail by depositing H_2O ice on an aluminum plate at 180 K (results are similar using a borosilicate substrate) [28]. Micrographs were recorded as the ice film was warmed to 273 K over an interval of about 30 minutes. Results for one ice sample at temperatures from 200 to 230 K are shown in Figure 6. Individual particles can be observed at 200 K; particle sizes were in the range 2–8 μm with an average size of about 5 μm. As the temperature was increased to 215 K, the particle size increased somewhat and sintering started to occur as shown by the formation of contact bridges among the particles. At higher temperatures still, the sintering and consolidation continued until at 230 K it becomes difficult to distinguish individual particles and a definition of particle size becomes meaningless. Stereological analysis of the electron micrographs of H_2O ice at

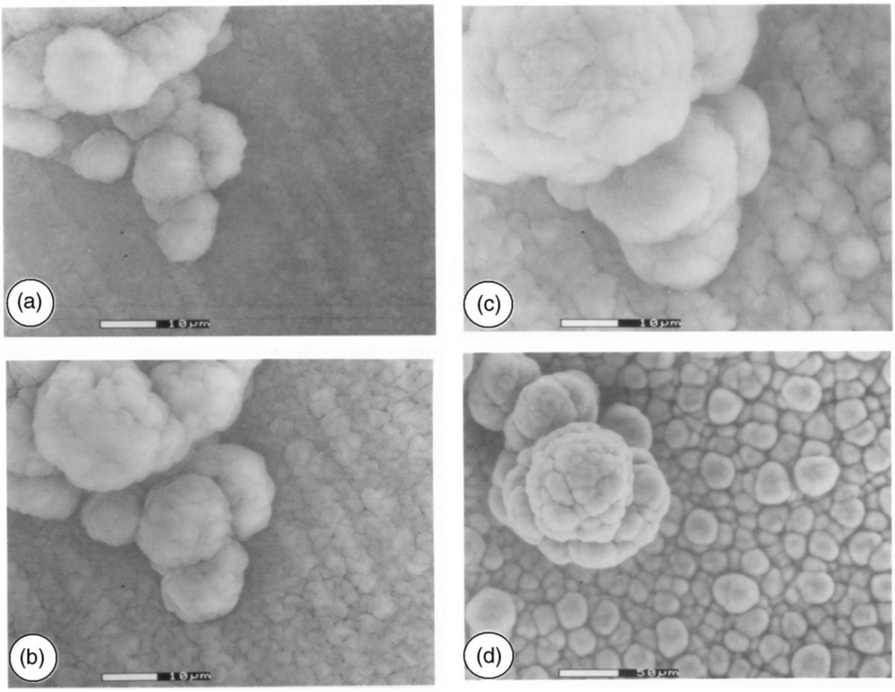

Figure 4. The figure is taken from Figure 1 of Keyser and Leu [28]. Electron micrographs of a HNO_3–H_2O ice film formed by vapor deposition onto a borosilicate substrate. Panels a–c show film growth during the deposition process at 197 K. Panel d shows effect of warming the film to 215 K. Total observation times since the start of deposition are 8 min (a), 11 min (b), 14 min (c) and 26 min (d).

200 K results in a bulk porosity of 0.40, which is in reasonably good agreement with values obtained using a photometrical method (see Section 3.3).

3.1.2.3. *Internal structure*. For some ice samples a micro–manipulator was used to move away portions of the outer surface in order to view the underlying internal structure. Figure 5(b), lower panel shows the results for H_2O ice deposited on a borosilicate substrate at 190 K. As seen in the figure, the internal ice structure comprises individual granules packed in somewhat irregular layers. In the side view panel in Figure 5(a), upper panel the thickness of the film can be measured; again, the layered packing is evident.

3.1.2.4. *Very low temperature deposition (93–133 K)*. In one series of experiments using the silicon substrate, H_2O ice was deposited at 133 K and then briefly annealed at 153 K. Typical results are shown in Figure 7. Thereafter, some ice samples were annealed to even higher temperatures, up to 183 K. At the latter temperature, hexagonal crystals with a size of about 1 µm developed. The shapes of these crystals are similar to those seen on borosilicate substrates (see above). The phase transitions observed in this study are consistent with those observed using X-ray diffraction, electron diffraction, and calorimetric techniques, where both cubic and hexagonal ices have been found to exist at 183 K [1].

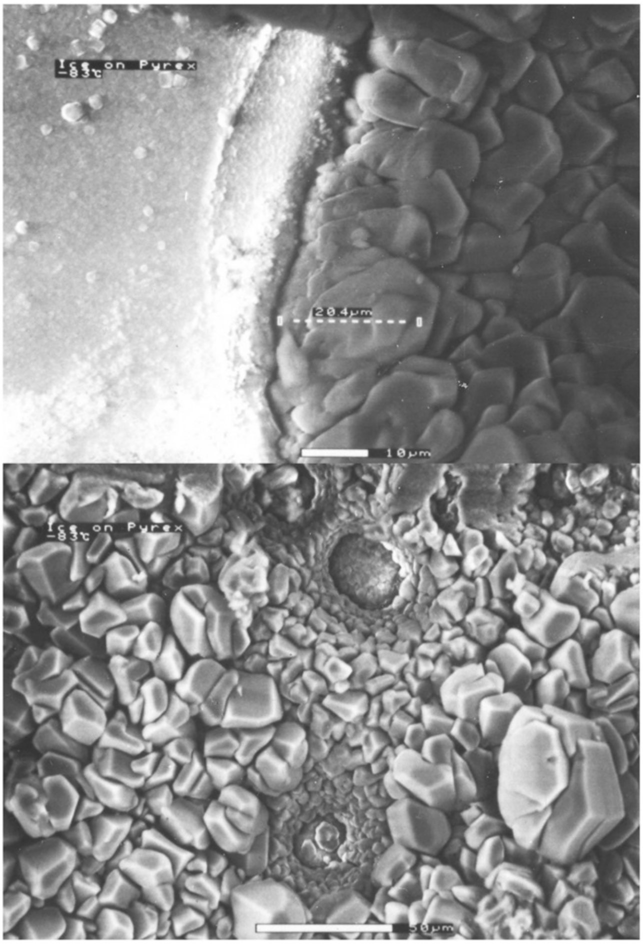

Figure 5. Electron micrograph of an H_2O ice film formed by vapor deposition onto a borosilicate substrate with (a) side and (b) top views.

In another series of experiments, we deposited ice on silicon and borosilicate plates either at 93 K or at 123 K. Then we annealed the samples at warmer temperatures, up to 173 K, under continuous observation. By using a resolution of about 0.1 μm, we found that the ice films were composed of very small amorphous particles of 0.2–0.4 μm at 93–123 K and granules of about 1 μm at 163–173 K. In general the granule sizes on the silicon surface are slightly smaller than those on a borosilicate surface, no doubt because of the difference in surface roughness of these materials. At these low deposition temperatures, micropores may be present inside the particles (see Section 3.2).

As discussed in the Introduction, Section 1.3, our ESEM data (~0.3 to 1 μm) are somewhat consistent with the Saturnian results (~1 to 5 μm). However, the grain sizes of ices on Jupiter's satellites (~10 to 100 μm) are substantially greater than those of our data (~0.3 to 1 μm) at relevant temperatures (120–150 K). Possible explanations have been discussed previously [21].

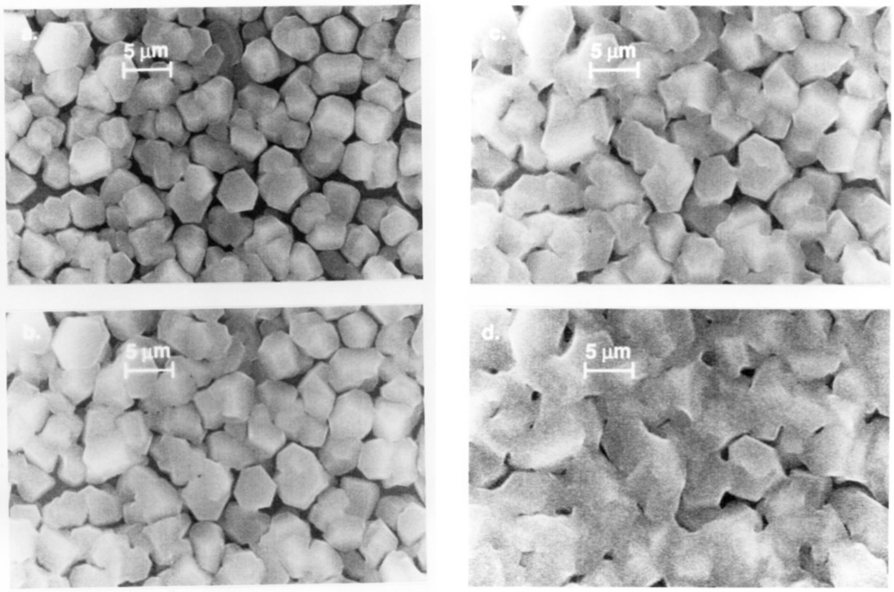

Figure 6. Electron micrograph of an H_2O ice film formed by vapor deposition on a polished aluminum plate at 180 K and them warmed to the temperatures indicated: (a) 200 K; (b) 215 K; (c) 220 K; (d) 230 K. See text for further discussion.

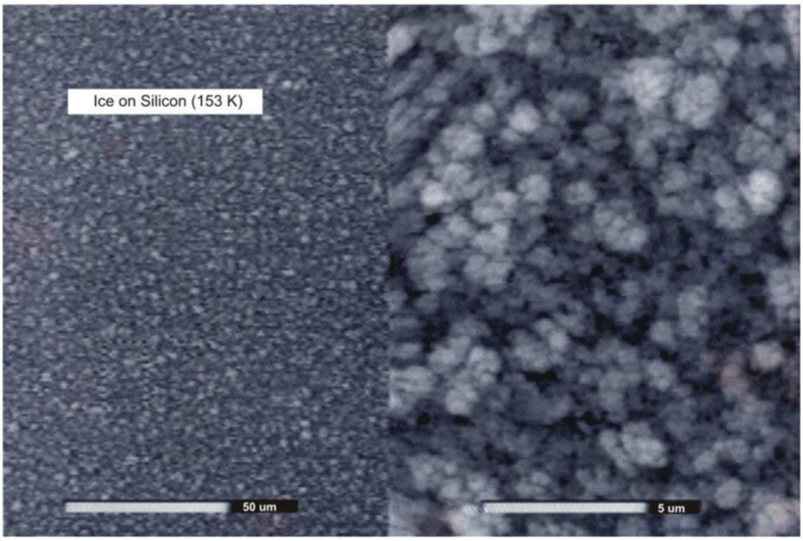

Figure 7. Environmental scanning electron micrograph of H_2O ice deposited on silicon at 133 K and then annealed at 153 K.

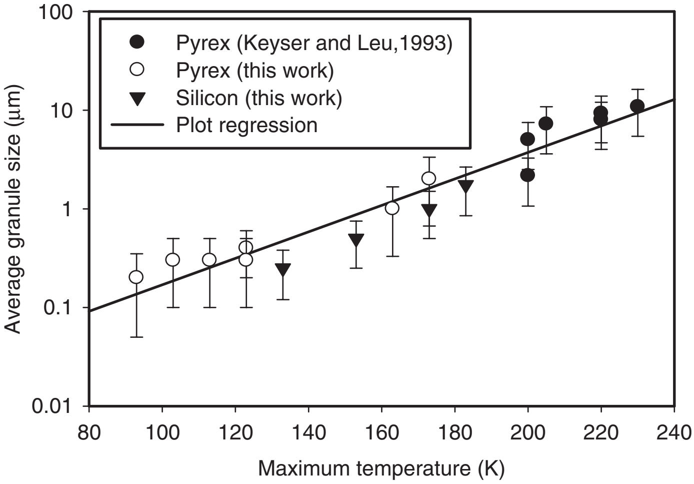

Figure 8. Average grain sizes (in units of µm) versus maximum temperature (in units of K).

3.1.2.5. *Granule size as function of temperature.* The average granule size correlates well with the maximum temperature (the higher of the deposition or annealing temperature) [21,28,29]. Figure 8 summarizes the relation between grain size and maximum temperature. Using a linear regression, we obtain the relationship

$$\log d = -2.11 + 0.0134\mathrm{T} \tag{7}$$

where d is the mean granule size in µm and T is the maximum temperature in degrees K. This relation is valid for thin ice films in the temperature range 90–230 K.

3.1.2.6. *Surface areas from particle size observations.* The ESEM experiments provide direct information on the sizes of the granules that make up the ice films. These sizes can be used to calculate the total area contributed by the external surfaces of the individual granules by using [30]:

$$S_\mathrm{g} = 6/\rho_\mathrm{t} d \tag{8}$$

where S_g is the specific surface area in $\mathrm{cm^2\,g^{-1}}$, ρ_t is the true density of the solid in $\mathrm{g\,cm^{-3}}$, and d is granule size or diameter in cm for spherical particles. Equation (8) is exact for spherical or cubic granules; for irregular granule shapes, it can be taken as an approximation. The relation is valid for a narrow granule size distribution about d. Surface areas calculated using Equation (8) will be compared with surface areas obtained from BET analyses of adsorption isotherms in Section 3.2.5.3.

3.2. *Surface area measurements using the BET method*

3.2.1. *Adsorption cells*

U–shaped Pyrex and quartz adsorption cells about 90 $\mathrm{cm^3}$ in volume were used to prepare ices by vapor deposition at a known temperature [21,29]. The cell design is shown

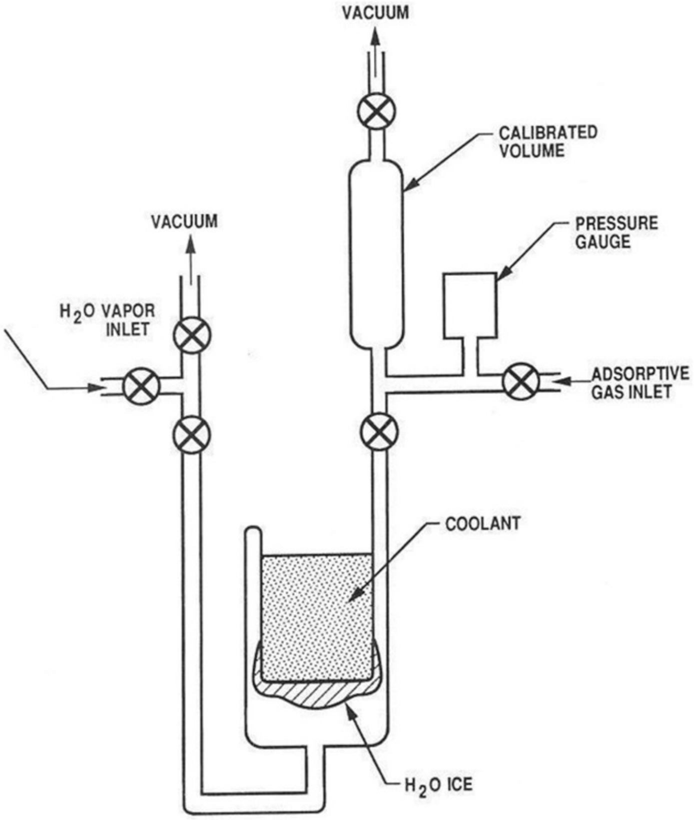

Figure 9. Schematic diagram of the BET adsorption apparatus.

schematically in Figure 9. Pure H_2O vapor or a mixture of H_2O and HNO_3 vapors was passed from a constant temperature reservoir into the adsorption cell. Prior to deposition, the liquid in the reservoir was out–gassed by purging with a stream of He and then evacuated. Flow rates of the vapors were controlled by using a glass–Teflon needle valve and calibrated by measuring the pressure drop in a known volume. Total pressure was 25 mtorr or less. Ices were deposited on the exterior of a cylindrical cold surface located in the exit arm of the cell. This design ensured that the vapors deposited first on the coldest glass surface. The ice formed on the bottom of the cold cylinder with small amounts extending as high as 3.5 cm along the sides depending on the deposition temperature. Most of the ice was deposited over a geometric area of about 30 cm^2 with a maximum thickness of 2–3 mm at the center of the cold cylinder. Average thickness calculated from the total weight, bulk density, and glass substrate geometric area ranged from 120 to 540 μm for H_2O ice and from 60 to 410 μm for HNO_3–H_2O ices. Liquid nitrogen, organics and liquid nitrogen slush, solid CO_2 in alcohol, and salted water ice were used to maintain constant temperatures between 83.5 and 261 K. Coolant levels were kept above the ice level on the cold cylinder. In some experiments the ice samples were annealed at higher temperatures by adjusting the amount of coolant in the reservoir.

3.2.2. *BET method*

Surface areas were measured by using the Brunauer, Emmett, and Teller (BET) method to analyze adsorption isotherms obtained at 77.2 K [30]. The U-tube was submerged in liquid nitrogen and isotherms were determined volumetrically by expanding from calibrated volumes maintained near 295 K. Adsorptive gases were N_2, Ar and Kr. In some experiments two adsorbates were used on the same sample to check for consistency of results. Nitrogen and Ar isotherms were corrected for nonideal gas behavior. In the case of Kr, the nonideal gas corrections were negligible at the pressures used; however, corrections were made for thermal transpiration between the cold adsorption cell and the room temperature section of the apparatus [31]. In addition, the measurements were corrected for the surface areas of the blank cells, which were determined in separate adsorption experiments. These areas are about a factor of 2 larger than those calculated from the cell dimensions, indicating apparent surface roughness of both the borosilicate and quartz cells. The dead space (cell volume minus ice volume) in the adsorption cell was determined before or after each experiment by using He. Calibrated capacitance manometers with full scale ranges from 10 to 1000 torr were used for the isotherm measurements. Adsorption and desorption isotherms were determined by serial addition and removal of the adsorptive gases. The procedure and calculations were checked against a γ-Al_2O_3 sample of known surface area. The measured area was within 3% to about 20% of the known area. At the completion of each run, the ice sample was warmed and collected by vacuum distillation for weighing and, in the case of HNO_3–H_2O ices, for determination of total acid by standard acid–base techniques.

3.2.3. *Ice temperatures*

During the deposition and annealing, the temperature was monitored by using a thermocouple immersed in the coolant bath. The temperature of the cooled glass surface inside the evacuated adsorption cell was measured in separate experiments by using a thermocouple attached to the surface with high thermal conductivity silicone grease. These measurements were carried out at coolant temperatures from 77 to 255 K. Near 77 K, the measured temperature was about 8 K higher than the coolant temperature; and near 195 K, it was about 4 K higher. Both calculation and experiment indicate that the true ice temperature is within 1–5 K of the glass-surface temperature [29]. The temperatures reported are the actual glass-surface temperatures. Estimated errors in the quoted temperatures are -2 K to $+6$ K.

3.2.4. In situ *measurements using a U-shaped flow-tube reactor*

A U–shaped fast–flow reactor was used to measure surface areas of ice films deposited from water vapor in a helium carrier by using a sliding injector [27]. The apparatus is shown schematically in Figure 10. The reactor was made of borosilicate tubing 40 cm in length and 2.50 cm inside diameter. The injector, also made of borosilicate tubing was 100 cm in length and 1.25 cm outside diameter; it was heated by passing a large flow of nitrogen gas through an outside jacket in order to prevent ice condensation inside the injector. The ice film was prepared by moving the injector from the bottom (downstream end) to the top of the flow tube. Temperature was measured by using a pair of thermocouples attached to the wall. Solid CO_2 plus methanol slurry or liquid nitrogen was

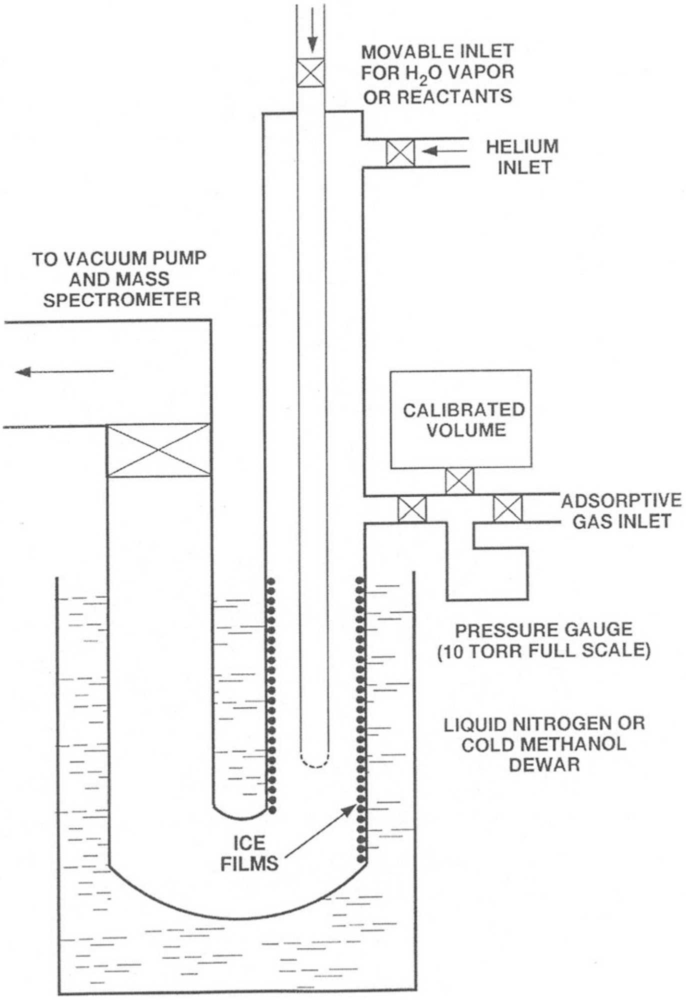

Figure 10. Schematic diagram of the BET adsorption apparatus coupled to a mass spectrometer for uptake measurements of HCl vapor on ice substrates.

used as a refrigerant. Since in these studies the ice samples were entirely surrounded by low–temperature surfaces, the ice temperatures reported are the measured thermocouple temperatures. Flow rates of water vapor in helium were controlled by using a stainless steel needle valve and read on a calibrated mass flow meter. The mass of ice deposited in the flow reactor was calculated from the flow rate and duration of the deposition. The thickness, h, of the ice films ranged from 1.04 to 47.4 μm and was calculated from the mass, m, the bulk density, ρ_b (see Section 3.3.1), and the underlying cylindrical geometry:

$$h = m/2\pi r_o L \rho_b \tag{9}$$

Surface areas were measured by using the BET method to analyze adsorption isotherms obtained at 77.2 K (see Section 3.2.1). The U-tube was submerged in liquid

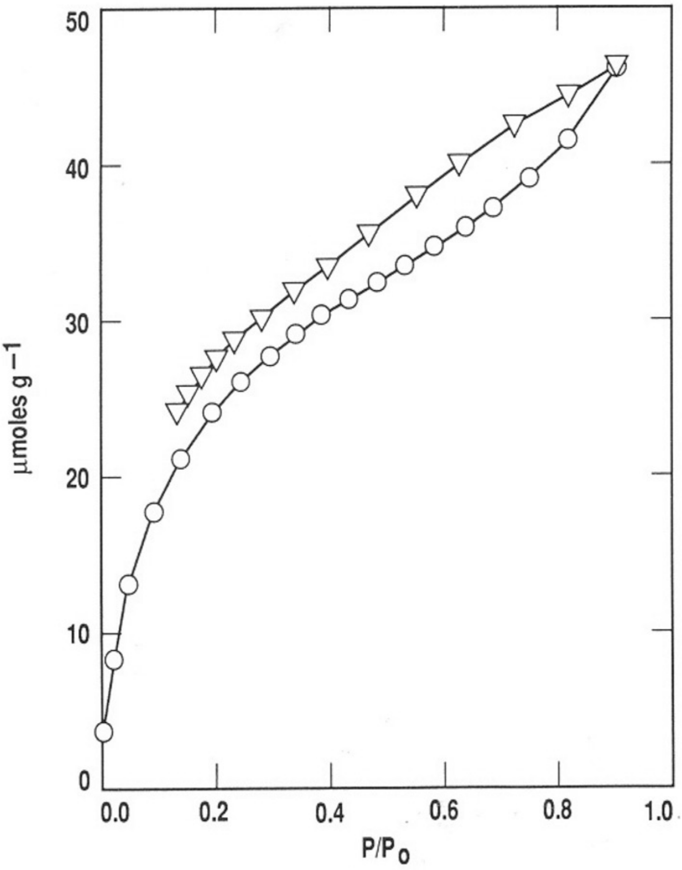

Figure 11. Adsorption–desorption isotherm of Kr on 0.716 g of HNO_3–H_2O ice (52.4 wt%) formed at 200 K; open circles, adsorption; open triangles, desorption.

nitrogen, and isotherms were determined volumetrically by expanding from a calibrated volume of 519.6 cm^3 maintained at room temperature. The adsorptive gas used was Kr. The pressure measurements were corrected for thermal transpiration between the cold adsorption cell and the room temperature section of the apparatus. Nonideal gas corrections were negligible. The surface area measurements were corrected for the surface area of the blank cell, which was determined in a separate experiment. The error limit of these measurements was estimated to be about ±100 cm^2.

3.2.5. *Results of surface area measurements*

Figure 11 shows a typical Kr isotherm on HNO_3–H_2O ice formed at 200 K [29]. The isotherm is continuous with no sharp changes in slope below the saturation pressure; the shape is approximately Type II with some hysteresis evident in the desorption branch. N_2 isotherms were similar as were isotherms observed for pure H_2O ices. Surface areas were obtained from BET plots such as those shown in Figure 12 for Kr adsorbed on H_2O ices

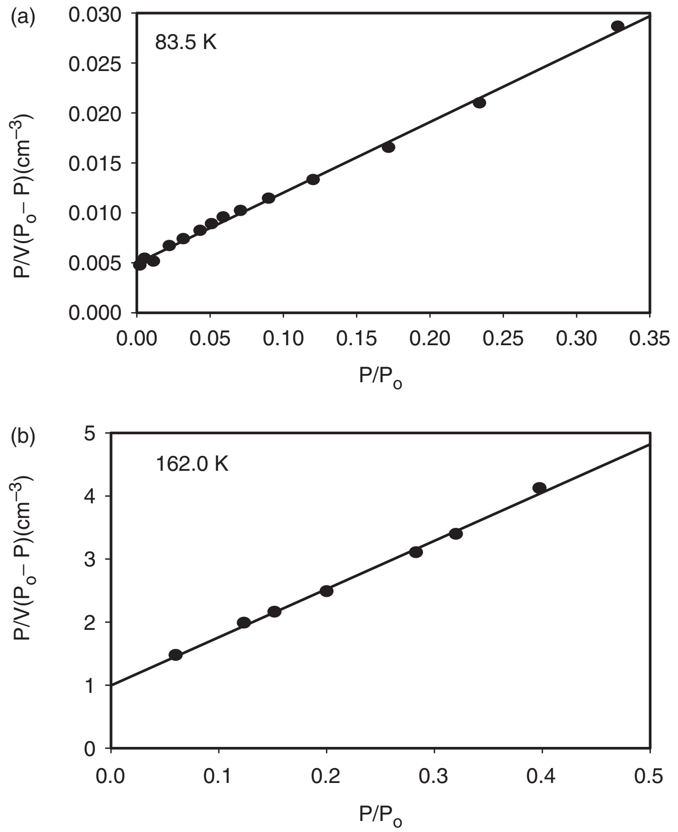

Figure 12. BET plot for Kr on (a) 0.6036 g H_2O ice mass at 83.5 K and (b) 0.6437 g H_2O ice mass at 162.0 K.

formed at 83.5 K and 162.0 K. As shown in Figure 12, the amount of Kr adsorbed at 83.5 K is almost two orders of magnitude greater than that at 162.0 K. Ice deposited at the lower temperature has a much greater adsorption capacity, and this implies a much larger surface area. The BET plots were linear between relative pressures of about 0.05 and 0.40. Linear regression of these plots yields a slope and intercept from which surface areas can be obtained. We obtained $118.8 \pm 3.2\,m^2\,g^{-1}$ at 83.5 K and $0.89 \pm 0.03\,m^2\,g^{-1}$ at 162.0 K. The errors are one standard deviation.

Comparisons using two different adsorbates on the same sample were made between N_2 and Kr, and between Ar and Kr; the measured surface areas agree within 15%. This agreement plus the smooth nature of the isotherms is evidence that under our experimental conditions no unusual interactions occur between the adsorbate molecules in the ices. This excludes any significant interference from, for example, hydrate or clathrate formation.

Tables 1 and 2 summarize the surface area results. For identical experimental conditions, the scatter in some of the results is relatively high; this has been observed previously [32] and may be due to random variations in the crystal dislocations and the pore structures of the growing particles. From Table 2 it is evident that there is no strong

Table 1. BET surface areas of H_2O ices.[a]

Maximum temperature, K[b]	Mass, mg	Deposition rate, mg min^{-1}	S_g, m^2 g^{-1}	Reference
77	19.7–119	1.6–2.4	325 ± 56	c
83.5	47–604	1.5–11.7	102 ± 27	d
85	226–513	2.0–8.5	250 ± 3	e
101	51.4–141	8.28–21.9	52.5 ± 15	d
121	29.9–408	2.75–22.6	17.6 ± 3.2	d
132	57.4–787	6.42–112	4.96 ± 1.76	d
150	88–634	3.42–10.5	0.87 ± 0.13	d
154	134–1069	3.32–127	0.75 ± 0.14	d
160	76.1–644	8.11–11.7	0.77 ± 0.29	d
178	65.3–217	3.13–6.72	0.69 ± 0.21	d
196	18.7–379	1.9–3.5	0.60 ± 0.41	c
200	724–1025	6.3–9.0	10.8 ± 5.7	e
201	178–673	5.94–68.2	0.52 ± 0.21	d
210	~1000	–	1.47	e
220	~1000	–	0.64 ± 0.27	e
230	~1000	–	0.230	e
256	329–573	21.9–190	0.43 ± 0.16	d
261	271–574	50.1–143	0.22 ± 0.06	d

[a] Errors are one standard deviation. [b] Deposition temperature or maximum annealing temperature. [c] Reference [27]. [d] Reference [21]. [e] Reference [29].

Table 2. BET surface areas of HNO_3–H_2O ices.[a,b]

Maximum temperature, K[c]	Wt% HNO_3	Mass, mg	Deposition rate, mg min^{-1}	S_g, m^2 g^{-1}
85	42.2	485	8.0	224 ± 6
85	75.9	906	12.0	176 ± 2
200	39.2	445–742	3.7–14.8	4.1 ± 0.9
200	52.9	570–1043	6.0–23.2	3.6 ± 1.4
200	63.9	152	1.27	2.1 ± 0.2
200	81.8	504–640	8.3–9.2	8.0 ± 3.7
210	53.1	~800	–	0.343
220	53.1	~800	–	0.462
230	53.1	~800	–	0.285

[a] Reference [29]. [b] Errors are one standard deviation. [c] Deposition temperature or maximum annealing temperature.

dependence of area on the HNO_3–H_2O ice composition from 39 wt% to 64 wt%; however, at 82 wt% the area appears to be significantly higher.

3.2.5.1. *Effect of deposition rate and sample mass.* Figure 13 summarizes the effect of deposition rate and sample mass on the observed surface areas at various temperatures. The areas appear to be independent of the H_2O deposition rate (1.5–190) mg min^{-1} and ice mass (30–1070) mg within experimental error limits, typically a few percent

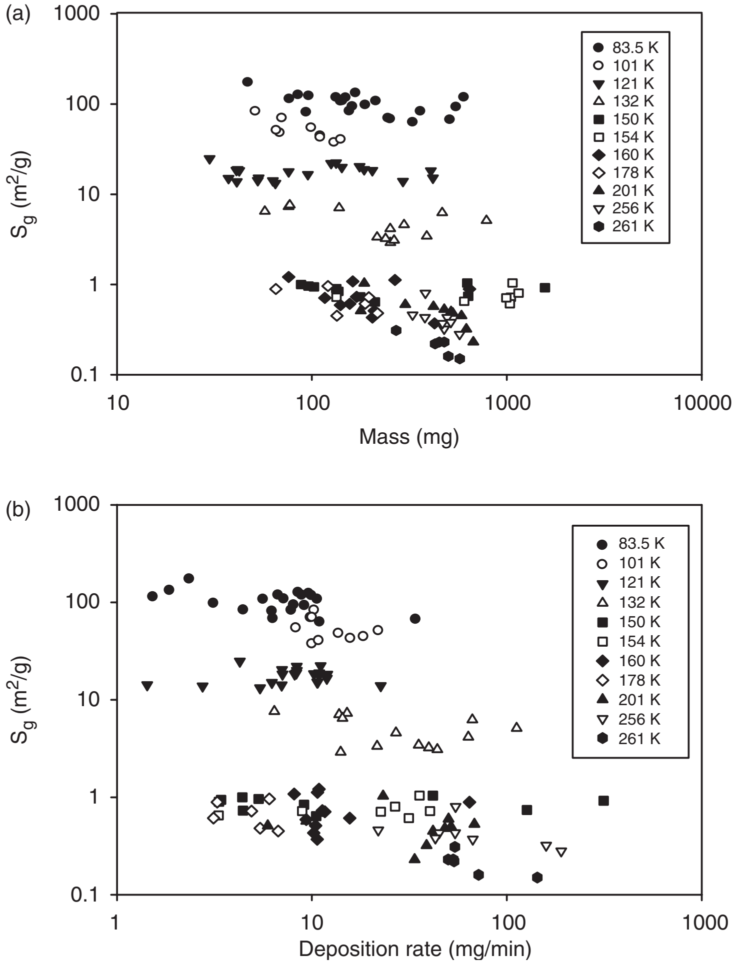

Figure 13. (a) Specific surface area ($m^2\,g^{-1}$) versus deposition rate ($mg\,min^{-1}$) and (b) specific surface area ($m^2\,g^{-1}$) versus mass (mg). Data are taken from Reference [21].

(1 standard deviation). However, this independence is not observed at larger ice masses (thicknesses). For example, at deposition temperatures of 154 and 201 K, the measured areas exhibit a positive correlation with ice mass above ~1000 mg (~1.3 mm thick) and ~700 mg (~0.9 mm thick), respectively [21]. This behavior may be due to a sharp increase in the internal porosity of thicker ice matrices and pore filling (see Section 3.2.5.4 below).

3.2.5.2. *Temperature dependence of surface areas.* Figure 14 summarizes the temperature dependence of H_2O ices. Some samples were formed by deposition at one temperature and not warmed or annealed; others were formed at low temperatures and then annealed at higher temperatures for 15–60 minutes. The temperatures plotted are either the deposition temperature or the highest annealing temperature of the ice sample. There was no significant effect of annealing time except at the highest temperatures studied: 265 K for

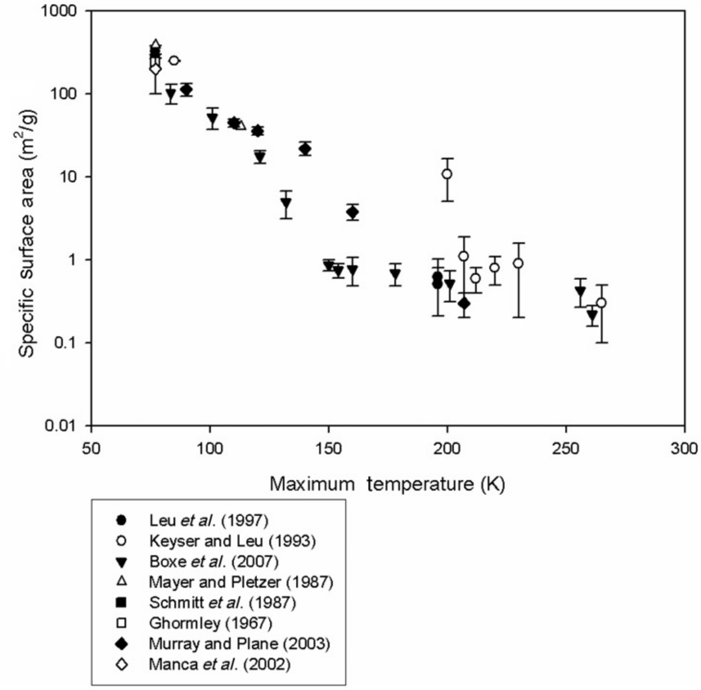

Figure 14. Specific surface area ($m^2 g^{-1}$) of H_2O ice versus maximum temperature (K).

H_2O ices and 250 K for HNO_3–H_2O ices; at these temperatures the areas decreased over time.

We also conducted a series of five experiments by depositing H_2O ice on substrates at 83.5 K and then annealing to about 180 K. In these cases, the average surface area was measured to be ~1.1 m^2g^{-1}. The data is consistent with the surface areas determined for ices deposited near ~180 K. This value is almost two orders of magnitude smaller than surface areas of ices formed at 83.5 K and not annealed. These observations suggest that the maximum temperature (or annealing temperature) that these ices encounter in their thermal history plays a major role in determining their surface areas.

It is evident from the figures that the ice surface areas are very sensitive to temperature. Water ice surface areas decrease sharply from several hundred $m^2 g^{-1}$ at 77 K to about 1 $m^2 g^{-1}$ near 150 K; at higher temperatures the areas decrease slowly to about 0.2 $m^2 g^{-1}$ at 261 K. This suggests that a phase transition from amorphous to cubic form occurs near 150 K and another transition occurs from amorphous and cubic to hexagonal form near 200 K. This observation is consistent with observations reported in the literature [1]. The HNO_3–H_2O ice samples show similar temperature sensitivity.

In some cases large decreases in surface areas were observed for ices formed at 200 K and then annealed at 210 K or higher, see Table 3, columns 2 and 3. These large decreases in surface areas with no significant change in bulk porosity (see Section 3.3) or external surface area suggests a mechanism that involves pore closure while maintaining approximately the same particle size and packing. As mentioned above phase changes and recrystallization may also play a role.

Table 3. Comparison of surface areas from BET, ESEM and pore size analysis.

Ice	Temperature, K	Surface areas, $m^2 g^{-1}$		
		S_g(BET)[d]	S_g(Ext)[h]	S_g(Int)[i]
H_2O	80[b]	180[e]	65	–
	200[b]	11.0[f]	1.7	2.3
	215[c]	0.78[f]	1.1	–
	220[c]	0.73[f]	0.94	–
	230[c]	0.63[f]	0.69	–
HNO_3–H_2O[a]	200[b]	2.7[g]	0.42	0.70

[a] 52.4 wt% HNO_3. [b] Ices formed by vapor deposition at temperature indicated. [c] Annealed by warming to the temperature indicated. [d] BET surface area. [e] References [21,29]. [f] Reference [29, Figure 4]. [g] Reference [29, Table 2]. [h] External surface area estimated from observed ESEM particle sizes by using Equation (8). [i] Internal surface area from pore size analysis.

The sensitivity to temperature is in general agreement with earlier work on H_2O ice as shown in Figure 14. Mayer and Pletzer [32] observed that the area decreased from about 400 to 40 $m^2 g^{-1}$ when the ice was formed at 77 K and 113 K, respectively; when the sample was warmed to 143 K, the area fell below their detection limit of 10 $m^2 g^{-1}$. Bar–Nun *et al.* [33] observed a significant decrease in surface area when the ice temperature was increased from 44 to 120 K. Adamson *et al.* [34] observed a large decrease in area when their ice samples were warmed to 203 K. Schmitt *et al.* [35] also observed a large loss of area when their vapor–formed ice was warmed from 77 to 190 K. In a recent work Murray and Plane [36] reported a strong temperature dependence of ice surface areas from 113 $m^2 g^{-1}$ at 90 K to 0.31 $m^2 g^{-1}$ at 207 K, in excellent agreement with the present results. However, their data at ~150–160 K are about 4 times greater than our results. Murray and Plane [36] deposited ice films at ~80 K and then annealed them at warmer temperatures. The different thermal histories of their ice samples and ours may play a role in this discrepancy. Manca *et al.* [37] also reported a value of 100–300 $m^2 g^{-1}$ at 77 K.

3.2.5.3. *Comparison of ESEM and BET surface areas.* The ESEM results can be used to estimate an average particle size and from this the outer surface area of the particles, S_g(Ext), can be calculated by using Equation (8) which holds for spherical particles. Near 80 K observed granule sizes were about 0.1 μm, which corresponds to an external area of ~65 $m^2 g^{-1}$; this is considerably lower than the 100–250 $m^2 g^{-1}$ obtained from the BET analysis. Particle sizes were found to vary from about 4 to 5 μm at 200 K to approximately 10 μm or more at 230 K (see Figure 8). However, we cannot use this procedure around 150 K due to the transition from amorphous ice to crystalline ice and possibly also due to smaller ice granules formed on the surface of the smooth silicon plate used in the ESEM experiment.

The BET areas are compared to the external surface areas in columns 3 and 4 of Table 3. The external areas agree reasonably well with the BET values above 200 K. However, at 80 K and 200 K the external areas of the particles are, respectively, about a factor of 3 and 6 lower than the BET surface areas. These results suggest that the annealed ices are composed of nonporous particles and that the BET surface areas of these annealed ices are equivalent to the external areas of the ice particles. The large difference between the BET and ESEM areas of the unannealed ices at 80 and 200 K implies that the particles comprising these ices have internal porosity. This was tested by using the pore size analysis discussed in the next section.

3.2.5.4. *Pore size analysis.* Pore size distributions were calculated for some of the unannealed ices deposited at 200 K. This type of analysis is well established and the procedure has been described in detail [30,38]. Briefly the analysis involves the calculation of the amount of adsorbate evaporated or condensed during each of several relative pressure changes during desorption or adsorption while accounting for the varying thickness of the adsorbate on the pore walls. Details have been given earlier [29]. This analysis yields pore or internal surface areas, $S_g(\mathrm{Int})$, which are given in column 5 of Table 3. For unannealed H_2O ice at 200 K, the sum of the external and internal surface areas is only about 35% of the BET area; for HNO_3–H_2O ice, the fraction is about 40%. This result implies that part of the BET value is due to pore filling. Pore filling is also most likely the cause of the difference at ~80 K.

3.3. *Ice porosity*

3.3.1. *Photometric measurements of ice bulk densities*

To further characterize these ices, bulk densities were measured. The bulk density, ρ_b, is the mass per unit substrate volume. Where the substrate volume includes all voids between the ice particles and all pores within the particles. The true density, ρ_t, is the mass per unit volume of actual solid material, excluding all voids; it is the density of a perfect single crystal. X-ray structure data give values of 0.925, 0.931, and 0.94 g cm^{-3} for the true densities of hexagonal ice, cubic ice and amorphous ice, respectively [1,2]. A value of 1.625 g cm^{-3} has been measured for the true density of NAT ice [39]. Because the packing of the ice particles usually includes voids and can be random and irregular, the bulk density of vapor-deposited ice is expected to be less than the true density. The porosity, θ, is the fraction of the solid that is void; it is related to the bulk and true densities by:

$$\theta = 1 - (\rho_b/\rho_t) \tag{10}$$

To obtain bulk densities, ice volumes were measured photographically. The densities were then calculated from the measured volumes and sample masses. Cameras equipped with macro lenses were used to photograph the vapor-deposited ices. The resulting images were enlarged up to about 5 times actual size and volumes were calculated from these images. Details are given in previous publications [21,29].

3.3.2. *Ice porosities from results of bulk density studies*

The results of the bulk density measurements are summarized in Tables 4 and 5 for H_2O ices and for HNO_3–H_2O ices, respectively. Both vapor-formed ices have bulk densities much lower than the true solid densities. The results are independent of temperature from 83 to 263 K. This is in sharp contrast to the ice surface areas, which decrease markedly over this same temperature range. We infer from these results that similar packing patterns of ice granules with various sizes occur over this temperature range. The ice porosities have been calculated from the densities by using Equation (10).

As noted in the Introduction, Section 1.3, the phase curves derived from observations of the icy Galilean satellites have been used to analyze surface structure [16]. These models used Hapke's theory to analyze the 0.47 and 0.55 μm bands from Earth-based telescopic observations and from the Voyager mission. Buratti [17,18] concluded that the surfaces of Ganymede and Callisto consist of 80% and 90% of void space, respectively. Domingue and colleagues [19,20] observed that Europa has a much brighter surface than the other satellites, and therefore consists of ~96% of void space. We measure much lower

Table 4. Bulk densities and porosities of H_2O ices.[a]

Maximum temperature (K)	Bulk density, $g\,cm^{-3}$	Bulk porosity[b]
83.5	0.62	0.34
107	0.66	0.30
124	0.62	0.34
137	0.62	0.34
152	0.64	0.31
181	0.66	0.29
199	0.65	0.30
200	0.63	0.32
200	0.61	0.34
210	0.62	0.33
220	0.58	0.37
220	0.65	0.30
227	0.64	0.31
230	0.71	0.23
245	0.63	0.32
263	0.64	0.31
	$av = 0.64 \pm 0.03$	$av = 0.32 \pm 0.03$

[a] References [21,29]. [b] Calculated by using Equation (10) and a true density of $0.925\,g\,cm^{-3}$.

Table 5. Bulk densities and porosities of HNO_3–H_2O ices.[a,b]

Maximum temperature (K)	Bulk density, $g\,cm^{-3}$	Bulk porosity[d]
200	0.80	0.50
200	0.93	0.43
200	0.87	0.46
c	0.89	0.45
210	0.81	0.50
220	0.77	0.52
230	0.79	0.51
	$av = 0.84 \pm 0.06$	$av = 0.48 \pm 0.03$

[a] Reference [29]. [b] Composition of HNO_3 was (53.1 ± 0.3) wt%. [c] This sample warmed to an undetermined temperature above 200 K when solid CO_2 plus methanol partially removed prior to cooling to 77 K. [d] Calculated by using Equation (10) and a true density of $1.62\,g\,cm^{-3}$.

porosities (~32%) than the data (~80–96%) obtained from phase curve analyses of icy Galilean satellites. The difference has been discussed in details previously [21].

3.4. *Infrared spectrometry*

3.4.1. *Low-temperature infrared cell*

The low-temperature infrared stainless steel cell was mounted within the sampling compartment of a BOMEM Model 3.002 Fourier-transform infrared spectrometer. It comprised a sample substrate on which the ice films were deposited, a borosilicate capillary tube for regulating the flow rates of vapor mixtures, and a KRS–5 window for the transmission of the infrared beam into the stainless steel cell. A schematic diagram is shown in Figure 15 [40,41].

The sample substrate was a copper plate that was mechanically polished and then coated with a gold film to a thickness of about 1 micron in order to prevent any reaction between the copper and nitric acid. A small quantity of liquid nitrogen was used to cool the substrate while simultaneously an electric heater was used to keep the other parts of cryostat warmer. A chromel/constantan thermocouple, used for temperature measurements, was attached to the edge with halocarbon wax. Ice films were formed by condensing vapors on the cooled substrate; the amount of vapor deposited was measured by using the pressure drop from a constant volume of 2.22 L at room temperature. The infrared spectra were recorded over the range of 550–4000 cm^{-1} by using a globar light source, a potassium chloride beam splitter, and a liquid–nitrogen cooled MCT detector. A resolution of 1.0 cm^{-1} was used throughout; typically 20–40 scans were accumulated for each spectrum taken.

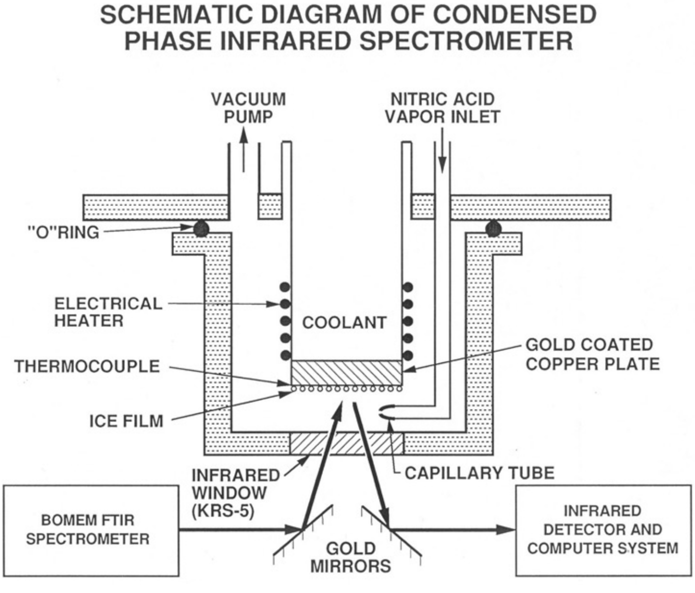

Figure 15. Schematic diagram of a condensed-phase reflectance infrared spectrometer.

Vapors containing water and nitric acid in the desired ratios were prepared by vaporizing aqueous solutions of nitric acid of suitable concentrations at 295 K. The vapors were condensed onto the surface of the substrate for infrared analysis. After infrared spectra were collected, ice films were warmed and their vapors were transferred into a U-tube for the determination of the stoichiometric ratio of water to nitric acid by a quadrupole mass spectrometer or acid-base titration. The measured partial pressures of water and nitric acid were calibrated by using literature vapor-pressure data and the calibrated data in our laboratory. The errors of these measurements were estimated to be about 20% [41].

3.4.2. *Results of infrared studies*

(1) Amorphous nitric acid ices were formed by condensing vapors from liquid HNO_3 solutions onto the cooled substrate at 153 K. The infrared spectra for compositions of $H_2O/HNO_3 = 1/1$, 2/1, and 3/1 are shown in Figure 16. The composition is confirmed by analysis. Spectra for $H_2O/HNO_3 = 2/1$ and 3/1 are very similar in several features, while the spectra of $H_2O/HNO_3 = 1/1$ shows rather distinct peaks at 1300–1700 cm^{-1}. Furthermore, the spectral bands over the wavelength range of 2000–4000 cm^{-1} are very broad. The spectra are similar to those obtained by Ritzhaupt and Devlin [42] and Koehler *et al.* [43]

(2) Spectra of NAM, NAD, α-NAT and β-NAT. The film of NAM was prepared by condensing vapors from a 70 wt% HNO_3 solution at 183 K. The substrate was then slowly warmed from 183 K to 243 K, and there was no change in the spectrum as shown in Figure 17(a). Similarly, NAD was prepared by the same method using a 66 wt% HNO_3 solution and its spectrum is shown in Figure 17(b). Both NAM and NAD spectra show some distinct features, and they are significantly different as shown in Figure 17(a) and 17(b). Both α-NAT and β-NAT were also obtained by a similar manner using a 61 wt% HNO_3 solution, and their spectra are shown in Figure 17(c) and Figure 17(d). These spectra also show some sharp features in the wavelength range of 500–4000 cm^{-1}. The infrared spectra are consistent with previously published data [42,43].

4. Theory of surface reaction and diffusion in porous ices

Ice films formed by deposition from the vapor phase have been widely used to simulate stratospheric cloud surfaces for laboratory measurements of reaction and uptake rates (see Section 2). To obtain intrinsic surface reaction probabilities that can be used in atmospheric models, we need to know the area of the film surface that actually takes part in the reaction. If the films are smooth and nonporous, the geometric area can be used, as was done in all of the early work using these ice films. However, studies of the morphology of films deposited under conditions (temperature, pressure, deposition rate, sample size, film thickness, substrate) similar to those used for the rate measurements show that the films have temperature–sensitive surface areas much larger than the geometric area and that they are composed of loosely consolidated granules with diameters of a few micrometers or less (see Section 3).

The large internal areas of such films consist of the surface areas of the individual ice granules and any internal pores in the granules themselves. The loose packing of the

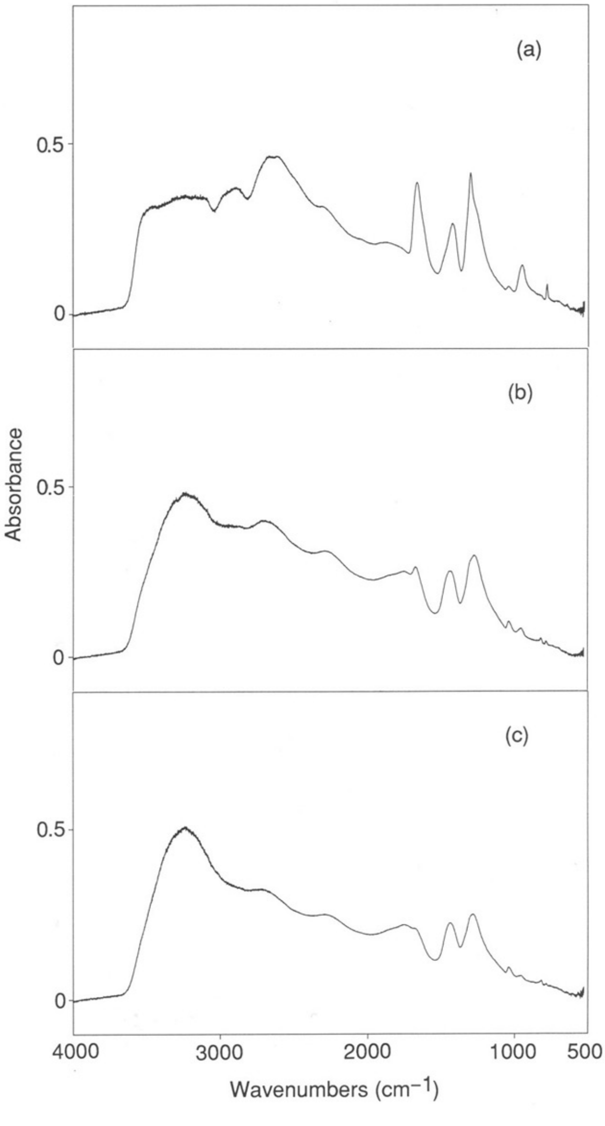

Figure 16. Infrared spectra of amorphous HNO_3–H_2O ices deposited and scanned at 153 K. The composition ratios of H_2O/HNO_3 are indicated as follows: (a) 1/1, (b) 2/1, and (c) 3/1.

granules makes these films highly porous and allows rapid gas phase diffusion into the interior of the film. For porous films, the observed reaction and uptake rates are affected by the internal surface area, and corrections, which account for the interaction of surface reaction and pore diffusion, are required in order to extract intrinsic reaction probabilities.

Here we discuss the interaction of surface reaction with diffusion and flow dynamics and apply the results to flow-tube heterogeneous reaction rate and uptake studies [44]. General procedures are developed to correct observed surface loss rates as needed. A more simplified empirical layer model is then presented and applied to experimental studies [45].

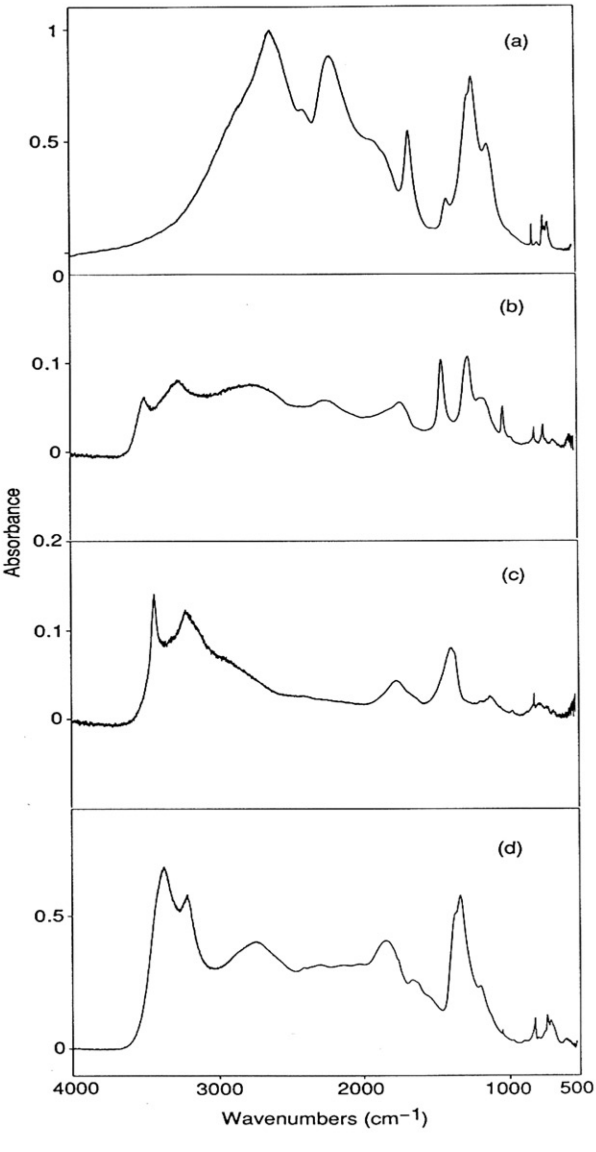

Figure 17. Infrared spectra of crystalline hydrates of HNO_3–H_2O ices: (a) NAM, (b) NAD, (c) α-NAT, (d) β-NAT.

Surface reactions in general comprise several stepwise and parallel processes. The following steps can occur during a heterogeneous reaction and are summarized schematically in Figure 18: (1) diffusive mass transport of reactants to the exterior surface of the solid (external diffusion); (2) adsorption–desorption of reactants at the surface; (3) diffusive mass transport of reactants within the interior of the porous solid (internal diffusion); (4) reaction on the surface or within the solid to form products; (5) adsorption desorption of products at the surface; (6) external diffusion of products

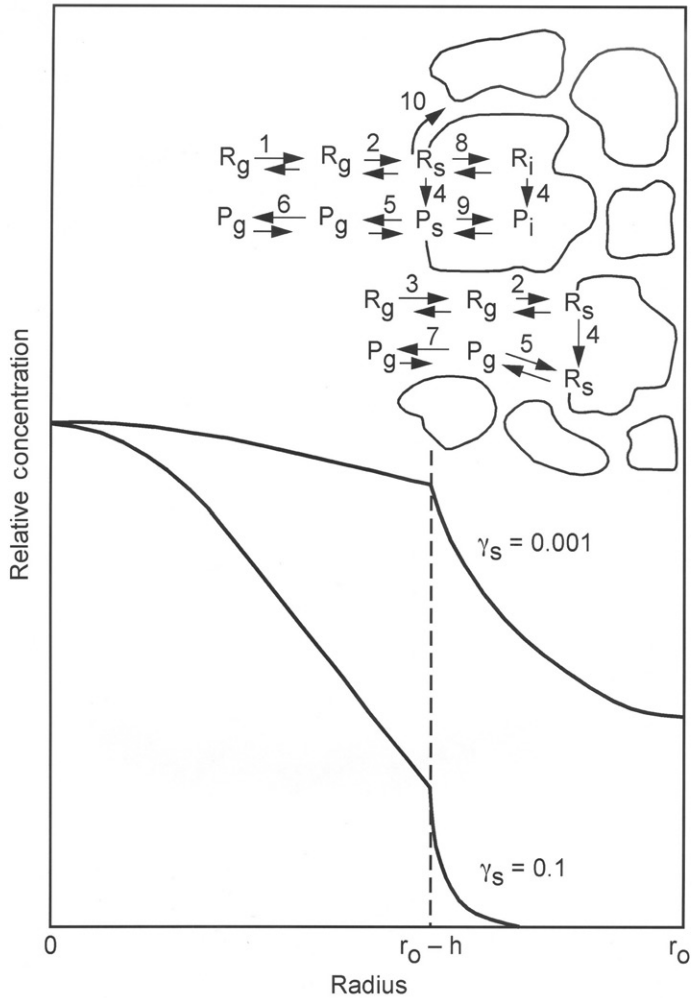

Figure 18. Diagram of a tubular reactor of radius, r_o, with a reactive solid of thickness, h, located on its inner surface.

away from the surface; (7) internal diffusion of products toward exterior of solid; (8) bulk, solid-state diffusion of reactants to interior of solid; (9) solid-state diffusion of products; (10) surface diffusion. The complete mechanism is highly complex, and in order to apply it some approximations are necessary. Generally the rates of some of the processes are much slower or faster than others, and this may be used as a basis for simplifying the mechanism. With respect to other processes in series, adsorption and desorption are usually rapid enough not to limit the reactivity of the surface, and we ignore them as a first approximation. However, it should be noted that the flow-tube experiments yield only an overall loss rate of labile species from the gas phase and, thus, cannot determine whether the rate-limiting process is adsorption or surface reaction. If adsorption is slow enough to become rate limiting, the quantity measured would be an adsorption or sticking rate rather than a surface reaction rate. The same correction procedure can be used as long as the system reaches steady state in a time short compared to the time of the experiment. Compared to gas-phase diffusion, the parallel steps of solid-state and surface diffusion of reactants are slow and need not be considered. At the low concentrations used, we can also ignore the effects of product diffusion in the gas phase. Product diffusion in the solid or on the surface is also neglected as a first approximation, but these processes or slow product desorption can affect surface deactivation. In addition, the rates of all homogeneous reactions are assumed to be negligible. The simplified mechanism consists, then, of steps 1, 3, and 4. In the sections which follow, these processes and their interaction with the fluid dynamics of a flow reactor are discussed in detail.

4.1. *External diffusion*

Under most experimental conditions used in flow reactors, observed surface decay rates are affected by the finite rate of diffusive mass transfer to the external surface and its interaction with laminar flow dynamics. Since this has been discussed in detail earlier [12,24,46–49] and the correction procedure has been validated experimentally [49], only a brief summary is presented here.

As a first approximation we ignore laminar flow and assume plug flow conditions so that the flow velocity, v, is independent of axial and radial position. We also ignore the effects of molecular diffusion and assume that the concentration of species C is independent of radial position. Under these conditions, the loss rate due to an irreversible first–order surface reaction in a reactor of volume, V, with uniform cross–section may be written

$$-v\mathrm{d}[C]/\mathrm{d}z = k'_{\mathrm{s}}(\mathrm{obs})[C]S_{\mathrm{total}}/V \tag{11}$$

where k'_{s} (obs), the observed surface rate constant in units of cm s^{-1}, is defined as the time rate of surface reaction per unit concentration, C, per unit surface to volume ratio. In Equation (11) reaction time has been converted to axial distance, z, by using the relation $z = vt$, which holds under the plug-flow conditions assumed. S_{total} is the total reactive surface area which for nonporous solids is usually taken as the exterior or geometric surface area. For a tubular reactor, $S_{\mathrm{total}}/V = 2/r_{\mathrm{o}}$, where r_{o} is the reactor radius. If we define the quantity $k_{\mathrm{s}}(\mathrm{obs}) = 2k'_{\mathrm{s}}$ (obs)/r_{o} with units of s^{-1}, Equation (11) becomes

$$k_{\mathrm{s}}(\mathrm{obs}) = -v\mathrm{d}\ln[C]/\mathrm{d}z \tag{5}$$

Equation (5) shows that under plug-flow conditions the surface rate constant can be obtained directly from the observed decay of C vs. reactor distance, z.

When laminar flow and diffusion are considered, the surface rate constant becomes [12]

$$k_{\mathrm{g}} = -\left(\frac{2D_{\mathrm{g}}}{r_0^2}\right)\left(\sum_{n=0}^{\infty} 2nB_{\mathrm{n}}/\sum_{n=0}^{\infty} B_{\mathrm{n}}\right) \tag{12}$$

where D_{g} is the gas-phase diffusion coefficient of the reactive species. The surface rate constant corrected for external diffusion, k_{g}, can be evaluated directly from Equation (12) since the coefficients B_{n} are functions of known quantities: D_{g} and the observed surface rate constant, $k_s(\mathrm{obs})$, obtained from Equation (5). For these calculations, a computer program was used to evaluate the sums in Equation (12) out to terms that were less than 1×10^{-10} of the total sum; usually less than 20 terms were required.

4.2. ***Internal diffusion***

When surface reactions occur in porous solids such as the ices studied here, gas-phase diffusion within the solid must be considered along with diffusive mass transport to the external surface. This is discussed here first in general terms; the results are then applied to the case of HNO_3–H_2O ices and tested experimentally.

4.2.1. *Interaction of surface reaction and diffusion in porous solids*

The theory [50–55] of internal diffusion and surface reaction in porous catalysts is well-known, but its application to flow-reactor studies such as those considered here was not given in detail before [44]. For porous materials, the reactive surface consists of both the external surface and any internal surfaces that can be reached by gaseous diffusion from the exterior of the solid. Under plug-flow conditions, Equation (11) becomes

$$-v\mathrm{d}[C]/\mathrm{d}z = k_t'[C](S_e + \eta S_i)/V \tag{13}$$

In Equation (13), k_t' is the true surface rate constant; S_e is the external surface area; S_i is the internal area, usually taken as the area measured by gas–adsorption experiments, the BET surface area (see Section 3.2); and η is the effectiveness factor which is discussed below. For a tubular reactor of radius r_o and length L with a solid substrate of thickness h deposited on its interior surface, the surface areas are

$$S_e = 2\pi(r_o - h)L(1-\theta)\sigma \approx 2\pi r_o L(1-\theta)\sigma \tag{14}$$

$$S_i = \pi[r_o^2 - (r_o - h)^2]L\rho_b S_g \approx 2\pi r_o h L \rho_b S_g \tag{15}$$

where θ is the porosity (ratio of void to solid volume) of the solid, σ is the roughness factor of the surface (ratio of actual external area to geometric area), ρ_b is the bulk density of the substrate, and S_g is the BET specific surface area of the substrate. The approximations are made for $r_o \gg h$ which is generally the case. With these substitutions Equation (13) becomes

$$k_s(\mathrm{obs}) = k_t[(1-\theta)\sigma + \eta h \rho_b S_g] \tag{16}$$

where $k_t = 2k_t'/r_o$. For most surfaces $\sigma \approx 2$ [51,52] and for the acid ices studied here, $\theta \approx 0.5$ (see below); thus, $(1-\theta)\sigma \approx 1$[1] and Equation (16) becomes

$$k_s(\mathrm{obs}) = k_t(1 + \eta h \rho_b S_g) \tag{17}$$

When we also include laminar flow and external diffusion in the gas–phase core of the reactor, Equation (17) becomes

$$k_g = k_t(1 + \eta h \rho_b S_g) \tag{18}$$

where k_g is given by Equation (12). In Equation (18), the quantity $(1 + \eta\rho_b S_g)^{-1}$ gives the correction for internal diffusion. A more complete derivation has been discussed [44].

The effectiveness factor, η, of a porous solid depends primarily on the relative rates of surface reaction and gas-phase diffusion; it is defined as the ratio of the observed diffusion-limited reaction rate to the rate that would be observed if diffusion were extremely fast. The effectiveness can also be thought of as the fraction of internal surface which takes part in the reaction. The variation of effectiveness with surface reactivity is illustrated in Figure 18, which gives concentration profiles for the reaction of $ClONO_2$ with HNO_3–H_2O ice under typical conditions used in flow reactors. In the central core of the reactor, the profile is determined by laminar flow, diffusion to the external surface and reaction at the surface. Within the porous solid, the controlling processes become Knudsen diffusion and surface reaction. The rapid falloff in concentration within a reactive solid ($\gamma = 0.1$) results in a low effectiveness factor of 0.072. In the less reactive solid ($\gamma = 0.001$), diffusion competes with surface reaction and a relatively high effectiveness factor of 0.65 results.

An expression for the effectiveness factor can be obtained by ignoring the substrate curvature since $h \ll r_o$ and approximating the substrate as a flat plate sealed on all surfaces except the top. Under these approximations, the effectiveness factor may be written [51,53,55]

$$\eta = \varphi^{-1} \tanh \varphi \tag{19}$$

$$\varphi = h(r_o k_t \rho_b S_g / 2D_e)^{1/2} \tag{20}$$

where φ is the Thiele modulus, a measure of the surface reaction rate relative to the porous diffusion rate, and D_e is the effective gas–phase diffusion coefficient of the reactive species within the porous substrate (see below). For inactive surfaces, k_t and, hence φ, are small; in this case tanh $\varphi \approx \varphi$ and $\eta \approx 1$. In other words, when the surface reaction is slow compared to pore diffusion, most of the internal surface participates in the reaction. Conversely for very active surfaces, k_t and φ are large and tanh $\varphi \approx 1$ and $\eta \approx \varphi^{-1}$; that is, when the surface reaction is fast compared to pore diffusion, only a small fraction of the internal surface is available for reaction.

4.2.2. *Analytical pore diffusion model*

Because it also determines η, the true surface rate constant, k_t, cannot be obtained directly from Equation (18). Instead we must simultaneously solve Equations (18), (19) and (20) by using experimental values for h, r_o, ρ_b and S_g. Separate experiments (described above) were carried out to measure these parameters in ices formed by vapor-deposition in a manner similar to that used to produce the substrates for flow-tube experiments. Typical data used for H_2O and HNO_3–H_2O ices are summarized in Table 6.

To solve these equations, we must also evaluate D_e, the effective diffusion coefficient. For this, a simple cylindrical pore model of the solid is introduced. The major assumptions of the model are (1) the internal surface area measured by the BET experiments is situated on the exterior of nonporous crystallites or small granules which make up the ice solid; (2) pores are the interstices among these granules; (3) on average the pores are cylindrical in shape with allowances for surface roughness and intersections; and (4) at the low pressures used in the present experiments the mean free path is large compared to the porous structure, and gas–phase transport within the porous solid is by Knudsen diffusion with modifications for porosity and pore deviousness.

Table 6. Typical values of parameters used to characterize vapor–deposited ices[a].

Parameter	Symbol, units	H_2O ice	$HNO_3{\cdot}3H_2O$ ice[b]	Comment
Specific surface area	S_g, $cm^2\,g^{-1}$	7.5×10^3	4.4×10^3	c
Bulk density	ρ_b, $g\,cm^{-3}$	0.63	0.82	c
True density	ρ_t, $g\,cm^{-3}$	0.925	1.62	d
Density ratio	ρ_b/ρ_t	0.68	0.51	–
Thickness	h, μm	96	74	e
Porosity	θ	0.32	0.49	f
Pore volume	V_g $cm^3\,g^{-1}$	0.51	0.60	g
Pore radius	r_p, μm	1.4	2.7	h
Tortuosity	τ	1.2	3.3	i
Effective diffusion coeff.	D_e, $cm^2\,s^{-1}$	0.51	0.55	j
av granule diameter	d, μm	8.6	8.4	k

[a]Deposited at 195 K and annealed at 205–220 K. [b]Composition was 53.0 wt% for HNO_3. [c]Measured. [d]From X-ray diffraction studies, [Ref. 1 for hexagonal ice and Ref. 39 for $HNO_3{\cdot}3H_2O$ ice]. [e]From Equation (9) for a sample mass of 1.0 g deposited over a length of 30 cm on inner surface of cylindrical flow tube of radius 0.88 cm. [f]From Equation (10). [g]From Equation (22). [h]From Equation (21). [i]Evaluated from best fit of data; see text. [j]From Equation (24) for $ClONO_2$ at 196 K and $\tau = 3.3$ for HNO_3–H_2O ices and $\tau = 1.2$ for H_2O ices. [k]From Equation (8).

For the cylindrical pore model, the average pore radius is

$$r_p = 2V_g/S_g \tag{21}$$

where V_g, the pore volume per unit weight, is given by

$$V_g = \theta/\rho_b \tag{22}$$

D_e may be written [44,52]

$$D_e = \theta D_k/\tau \tag{23}$$

where D_k is the Knudsen diffusion coefficient and τ is the tortuosity factor discussed below. Since $D_k = 2r_p\omega/3$ we have

$$D_e = 2\theta r_p\omega/3\tau \tag{24}$$

where r_p is the pore radius, θ is the porosity from Equation (10), and ω is the average molecular velocity given by:

$$\omega = (8RT/\pi M)^{1/2} \tag{25}$$

In Equation (25), R is the gas constant, T, the absolute temperature, and M, the molecular weight of the diffusing species.

In porous solids actual diffusive mass transfer can be slower than predicted because within these materials diffusion does not occur in straight-line paths nor in pores of uniform cross-section. To account for this, a tortuosity factor, τ, is introduced. Models of porous solids predict values for τ that are generally in the range 1–8. Usually the magnitude of the internal diffusion corrections are not very sensitive to the value of τ used [44]. For the vapor-deposited ices used here, τ was evaluated semi-empirically by observing the variation of the surface decay rates with sample thickness (see below). Typical values for the porosity, pore volume, pore radius, tortuosity, and effective diffusion coefficient are also given in Table 6.

Two general approaches can be used to solve the analytical model. First, if several data points are available, nonlinear regression can be used to fit the data by simultaneously solving Equation (18)–(20) with k_t and τ as fitting parameters. An example is given in Section 5.1.1.

Second, if only a few data points are available, a root finder can be used to correct the individual data points for the effects of the internal surface. In order to obtain this solution, it is convenient to eliminate k_t and define a new dimensionless parameter, Ω, which can be evaluated from experimental quantities. From Equation (20) we have

$$k_t = \left(2D_e\varphi^2\right)/\left(r_o\rho_b S_g h^2\right) \tag{26}$$

and substituting into Equation (18) we obtain

$$\Omega = \left(r_o\rho_b S_g h^2 k_g\right)/(2D_e) = \varphi^2\left[1 + \varphi^{-1}\tanh(\varphi)\eta h p_b S_g\right] \tag{27}$$

All of the parameters can be obtained experimentally or can be estimated. A root finder can then be used to determine the value, φ_o, for which the two sides are equal. The true rate constant, k_t, can then be calculated from Equation (18). An example of this type of calculation is also given below in Section 5.1.1.

4.2.3. *Layer model*

A more simplified model of vapor–deposited ices can be developed by considering them as made of ice particles stacked in layers [45]. This model is also based on the morphology studies using optical and electron microscopy and BET analysis presented above. In this approximation, the film comprises spherical granules stacked in layers. For the purposes of this discussion, we consider both an external and an internal film thickness and Equation (13) becomes

$$-v\,\mathrm{d}\ln[C]/\mathrm{d}z = \left(2k'_t/r_o\right)\rho_b S_g(h_e + \eta h_i) \tag{28}$$

where h_e and h_i are, respectively, the external and internal thickness of the film; the total thickness, h, is $h_e + h_i$. The external thickness is defined below. Using Equation (5) and noting that $(2k'_t/r_o) = k_t$ (see above), Equation (28) becomes

$$k_s(\mathrm{obs}) = k_t\rho_b S_g(h_e + \eta h_i) \tag{29}$$

After correcting for laminar flow and diffusion (Equation 12), we have

$$k_g = k_t\rho_b S_g(h_e + \eta h_i) \tag{30}$$

Using Equation (6) to convert k_g and k_t to reaction probabilities and noting that generally $\omega \gg r_o k$, we can write

$$\gamma_g = \gamma_t\rho_b S_g(h_e + \eta h_i) \tag{31}$$

The specific surface area can be written (Equation 8) in terms of the true density, ρ_t, and the granule diameter, d. If we take the external surface to be the upper half of the top layer of spherical granules,

$$h_e = d/2 \tag{32}$$

For simple cubic packing (SCP),

$$\rho_b = (\pi/6)\rho_t \tag{33}$$

$$h_i = d(N_L - ½) \tag{34}$$

where N_L is the number of granule layers. Substituting Equation (8) and Equations (32)–(34) into Equation (31) gives

$$\gamma_g = \gamma_t(\pi/2)[1 + \eta(2N_L - 1)] \tag{35}$$

The effectiveness factor, η, is given by Equation (19) and has been discussed above. In the case of the layer model, the Thiele modulus becomes

$$\varphi = (h_i/d)[3\rho_b/2(\rho_t - \rho_b)](3\tau\gamma_t)^{1/2} \tag{36}$$

where τ is the tortuosity factor discussed above and cylindrical pores are assumed (see Section 4.2.2).

In the layer model, the packing and, hence, the bulk density and tortuosity are independent of film thickness. Thus, Equation (19) and Equations (34)–(36) show that the observed film reactivity depends only on the number of layers, N_L. If the film morphology is such that the granule size remains approximately constant, N_L increases with thickness and a large change in reactivity can be observed as the thickness increases. However, if the granule size increases proportionately with the thickness, N_L remains constant and no variation in reactivity will be observed even though the film is highly porous. Between these two extreme cases, the granule size could increase less rapidly than thickness and a moderate change in reactivity would be observed.

The ratio of bulk to true density calculated from Equation (33) is 0.52; this is the value measured for $HNO_3{\cdot}3H_2O$ (NAT) [29]. However, for H_2O ice, the measured density ratio is 0.68 [29], which is close to the value of 0.74 predicted from a layer model comprising hexagonal close–packed (HCP) spheres, Equation (37) below. The same packing density would be observed in face–centered cubic packing. To model NAT ice, SCP can be used; however, for H_2O ice, HCP is a better approximation. For HCP, Equations (33)–(35) become [note 5 in Ref. 45]

$$\rho_b = (\pi/3)2^{-1/2}\rho_t \tag{37}$$

$$h_i = d\left[(N_L - 1)(2/3)^{1/2} + (1/2)\right] \tag{38}$$

$$\gamma_g = 3^{-1/2}\gamma_t\pi\left\{1 + \eta\left[2(N_L - 1) + (3/2)^{1/2}\right]\right\} \tag{39}$$

In the sections that follow these theoretical results are applied to experimental measurements of reaction probabilities, sticking coefficients and uptake on ices of interest in atmospheric chemistry.

5. Results and application of theory

Using the theory of surface reaction in porous ices, we have analyzed the results for several important atmospheric processes. These include: heterogeneous reactions of

$ClONO_2 + H_2O \rightarrow HOCl + HNO_3$ (3), $ClONO_2 + HCl \rightarrow Cl_2 + HNO_3$ (2), $HOCl + HCl \rightarrow Cl_2 + H_2O$ (4), and the uptake of HCl, H_2O and HNO_3. The ice substrates comprise either H_2O ice or HNO_3–H_2O ice. In addition, we also used the theory for the study of $ClONO_2$ and HNO_3 on solid powder substrates. These results are discussed in detail in the following sections.

5.1. *Reaction of $ClONO_2 + H_2O$ on HNO_3–H_2O ice*

5.1.1. *Experimental test of the analytical pore diffusion model*

The Thiele pore diffusion model predicts that if the internal surface participates in the reaction, the observed reaction rates will be sensitive to the substrate thickness over a certain range. This occurs because the resistance to pore diffusion measured by the Thiele modulus, φ, is directly proportional to the substrate thickness, h (Equation 20). Thus, for thin subtrates, φ is small and the effectiveness factor (Equation 19) approaches unity since $\tanh \varphi = \varphi$. In this case the rate constant expression (Equation 18) becomes linear in h. For thick substrates, φ is large and the effectiveness factor becomes proportional to h^{-1} since $\tanh \varphi = 1$ for $\varphi > 2$. In this case the rate constant expression becomes independent of h, and the observed rate constants should approach a limiting value as the substrate thickness is increased. This occurs obviously because the amount of internal surface is proportional to h, but its effectiveness is proportional to h^{-1}.

As a test of the pore diffusion model, rate constants for the reaction of $ClONO_2$ with H_2O:

$$ClONO_2 + H_2O \rightarrow HOCl + HNO_3 \qquad (3)$$

were determined on HNO_3–H_2O substrates that varied in thickness from about 15 μm to 120 μm [44,57]. Thickness was controlled by condensing mixtures of H_2O and HNO_3 vapors for varying amounts of time on the cold inner surface of a flow tube reactor; only one or two thicknesses were used per run. Details of the deposition procedure used to form the substrates and the methods used to obtain the rate data are given in Section 2.1.

Observed $ClONO_2$ decay rates are shown in Figure 19 for substrate thicknesses of 13 and 108 μm; the abrupt change in slope occurs at the point where the substrate thickness changes. All of the results are summarized in the first four columns of Table 7 and in Figure 20. The observed increase in reactivity with thickness shows that the HNO_3–H_2O ice substrates are indeed porous and that some portion of the internal surface is available for reaction. A nonporous solid with no solid–state diffusion should exhibit little or no variation in reactivity with thickness since only the external surface is available. Small changes in surface roughness are possible, but this cannot account for the large magnitude of the observed effect.

Nonlinear regression was used to fit all the data in Table 7 to Equation (18)–(20); the result is the solid line in Figure 20. This was calculated by allowing τ and k_t to vary and by using the values given in Table 6 for the other HNO_3–H_2O ice parameters. The best fit occurs for $k_t = 15.5 \pm 2.7\,s^{-1}$ and $\tau = 3.3 \pm 1.0$. The corresponding γ_t is $(1.32 \pm 0.31) \times 10^{-3}$. The errors are one standard deviation obtained from the regression.

As an additional check of the analytical pore–diffusion model, individual data points in Table 7 (columns 1 and 3) were corrected by using a root finder to solve Equation (27). The results are shown in columns 7–8 in Table 7 and agree very well with the nonlinear fit

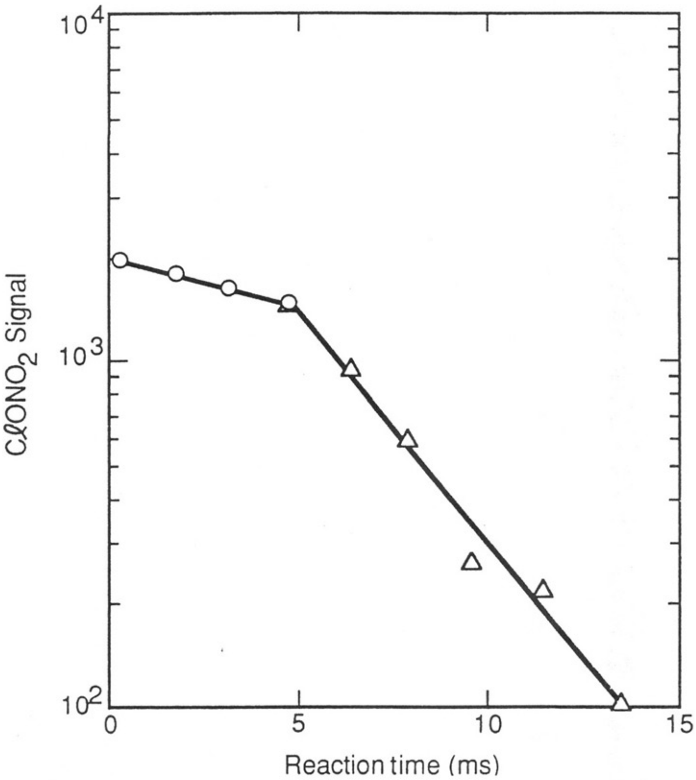

Figure 19. Observed $ClONO_2$ decay rates for two thicknesses of HNO_3–H_2O ice: open circles, 13 μm; open triangles, 108 μm.

Table 7. Effect of HNO_3–H_2O ice[a] thickness on $ClONO_2$ loss rates.

Thickness, μm	k(obs), s^{-1}	k_g,[c] s^{-1}	$10^3\gamma_b$[d]	φ[e]	η[f]	k_t,[g] s^{-1}	$10^3\gamma_t$[d]
13.0	54.2	55.8	4.75	0.220	0.984	9.94	0.847
17.3	70.8	73.5	6.25	0.299	0.971	10.4	0.887
29.0	176	194	16.4	0.682	0.869	19.2	1.64
59.1	215	242	20.4	1.255	0.677	15.7	1.34
72.8	260	300	25.3	1.733	0.542	19.7	1.68
91.2[b]	211	236	19.9	1.731	0.542	12.5	1.07
108	257	296	24.9	2.435	0.404	17.7	1.51
116	227	257	21.7	2.298	0.426	13.6	1.16
						av 14.9 ± 3.8	av 1.26 ± 0.32

[a] Composition was 45.5 ± 0.7 wt% HNO_3 unless otherwise indicated. [b] 37.6 wt% HNO_3. [c] Corrected for external diffusion by using Equation (12). [d] From Equation (6). [e] Obtained from Equation (27) by using the sample thicknesses given in column one with $r_o = 0.88$ cm and the HNO_3–H_2O ice parameters given in Table 6. [f] From Equation (19). [g] From Equation (18).

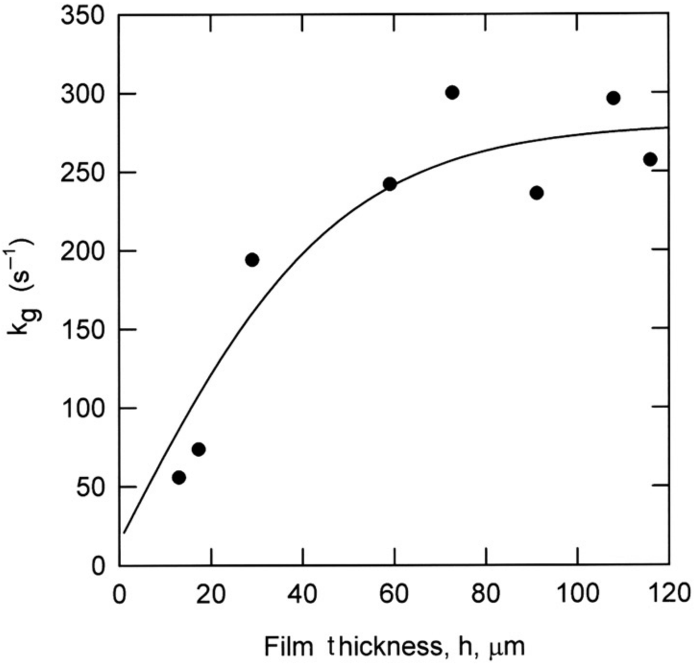

Figure 20. Plot of surface rate constants corrected for external diffusion, k_g, vs. substrate thickness, h (column 3 vs. column 1 of Table 7) for the reaction of $ClONO_2 + H_2O$ on HNO_3–H_2O ice. The line through the data is a nonlinear regression fit to Equations (18)–(20). The best fit gives $\tau = 3.3 \pm 1.1$ and $k_t = 15.5 \pm 2.7\,s^{-1}$; $\gamma_t = (1.3 \pm 0.3) \times 10^{-3}$. The errors given are one standard deviation obtained from the regression analysis.

shown in Figure 20. The standard deviation of the values is about 25% of the mean for a variation in thickness over nearly an order of magnitude. For these samples the correction factors (column 3 divided by column 7) vary from about 6 to 19. The good agreement among the corrected k_s values for such a large range of sample thickness and corrections verifies that the diffusion model can be applied to the ices studied.

5.1.2. *Experimental test of the layer pore diffusion model*

The layer model presented in Section 4.2.3 will now be used to analyze the same data discussed in Section 5.1.1. The reaction probabilities corrected for external diffusion, γ_g, are plotted vs. substrate thickness in Figure 21. The SCP layer model was used since it fits the HNO_3–H_2O ice substrates best. Nonlinear regression was used to fit the data. In addition to these equations, we need an expression that relates the number of layers, N_L, to the substrate thickness, h. Our morphology studies have shown that ice films formed by deposition from the vapor phase consist of micrometer-sized granules and that they increase in size with deposition time, thus, with thickness. An expression that best describes this behavior is of the form given by

$$N_L = a + b \log(h) \tag{40}$$

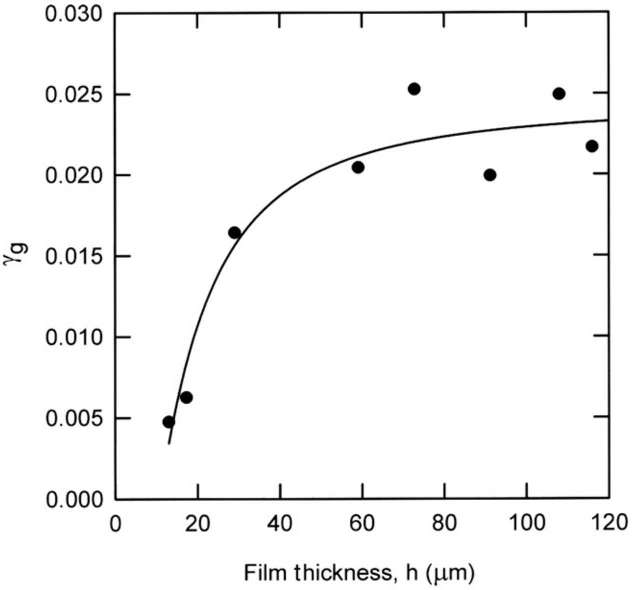

Figure 21. Plot of reaction probabilities corrected for external diffusion, γ_g, vs. substrate thickness, h (column 4 vs. column 1 of Table 7) for the reaction of $ClONO_2 + H_2O$ on HNO_3–H_2O ice at 196 K. The line through the data is a nonlinear regression fit of the layer model, with $\tau = 3.3$ and $N_L = a + b \log(h)$. The best fit gives $\gamma_t = (1.2 \pm 0.3) \times 10^{-3}$, $a = -11$, $b = 11$. The errors given are one standard deviation obtained from the regression analysis.

where the thickness, h, is expressed in micrometers. A value of 3.3 has already been determined for τ from the fit of the analytical model in Section 5.1.1. A regression analysis was carried out by using Equation (19) and Equations (35) and (36) with γ_t, a and b as fitting parameters. The result is the solid line in Figure 21 with $\gamma_t = (1.2 \pm 0.3) \times 10^{-3}$, $a = -11$ and $b = 11$. This expression for N_L is valid for h in the range 15–120 μm only. The value of γ_t obtained from the layer model agrees very well with the values obtained by using the full analytical model, see Figure 20 and column 8 of Table 7.

5.1.3. *Summary of results for $ClONO_2 + H_2O$ on HNO_3–H_2O ice*

The reaction was studied using the earlier version of the flow reactor [57]. The inner wall of the reactor was coated with HNO_3–H_2O ice and the substrate composition was analyzed using acid–base titration. The results are summarized in Figure 22. The reaction probability after correcting for external diffusion shows a strong dependence on substrate nitric acid composition [57].

5.2. Reaction of $ClONO_2 + H_2O$ on H_2O ice

5.2.1. *Application of the analytical model*

The reaction rate of $ClONO_2 + H_2O$, Equation (4) was also determined on H_2O ice substrates [58]. Because the product HNO_3 is adsorbed and can deactivate the ice surface,

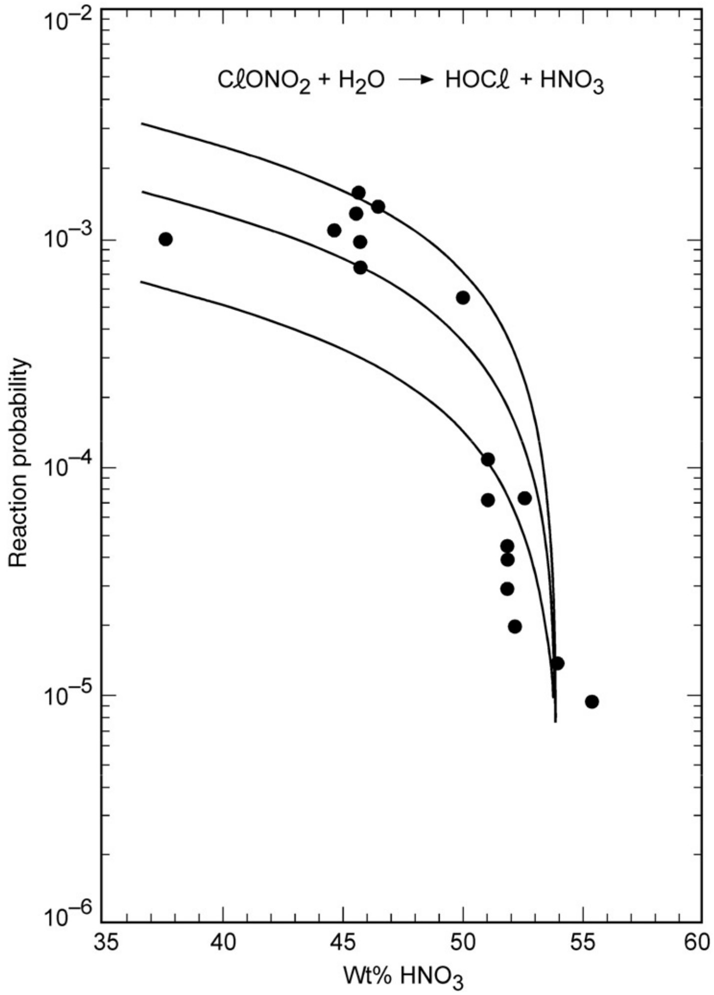

Figure 22. Summary of the data for the reaction $ClONO_2 + H_2O \rightarrow HOCl + HNO_3$ on HNO_3–H_2O ice surfaces. The reaction probabilities after corrections using the analytical model are plotted versus weight percents of HNO_3 in the substrate. The curves through the data are calculated from a model assuming that the substrate comprises a two–phase mixture of NAT and H_2O ice. Details are given in Leu *et al.* [57].

we used very low partial pressures of $ClONO_2$ near 1.4×10^{-7} torr. The temperature was 188 K. The results are summarized in Table 8 and Figure 23. In each experiment we first measured the $ClONO_2$ decay and then the growth of HOCl product. In general, the data obtained from the HOCl growth is equal to or smaller than that obtained from the $ClONO_2$ decay because of a small amount of surface deactivation by HNO_3 product.

The analytical pore diffusion model was used to correct these data for internal diffusion. Nonlinear regression was used to fit all the data in Table 8 to Equations (18)–(20); the result is the solid line in Figure 23. This was calculated by allowing τ and k_t to

Table 8. Reaction probabilities of $ClONO_2 + H_2O \rightarrow HOCl + HNO_3$ on H_2O ice[a].

Thickness (μm)	$ClONO_2$ decay			HOCl growth		
	$10^{-3}\ k_g$[b] (s^{-1})	$10^2\ \gamma_g$[c]	$10^2\ \gamma_t$[d]	$10^{-3}\ k_g$[b] (s^{-1})	$10^2\ \gamma_g$[c]	$10^2\ \gamma_t$[d]
3.7	0.574	4.88	0.360	0.448	3.83	0.247
4.2	1.10	9.14	1.01	0.891	7.47	0.719
8.6	1.39	11.4	1.45	0.725	6.12	0.508
9.0	0.782	6.59	0.577	1.34	11.0	1.37
9.2	1.03	8.58	0.904	1.56	12.7	1.73
10.6	1.18	9.77	1.12	1.22	10.1	1.18
18.9	1.26	10.4	1.24	1.58	12.9	1.76
24.8	1.64	13.3	1.86	1.69	13.7	1.94
25.7	1.50	12.3	1.63			
34.1	1.14	9.46	1.04			
			av[e] = 1.4 ± 0.4			av[e] = 1.6 ± 0.4

[a] A small amount of product HNO_3 could be adsorbed on the ice surface. [b] After correction for gas–phase axial and radial diffusion, Equation (12). [c] From Equation (6). [d] From HCP layer model, see text. [e] Av for film thicknesses greater than 10 μm because of possible deactivation from HNO_3 product on thinner films.

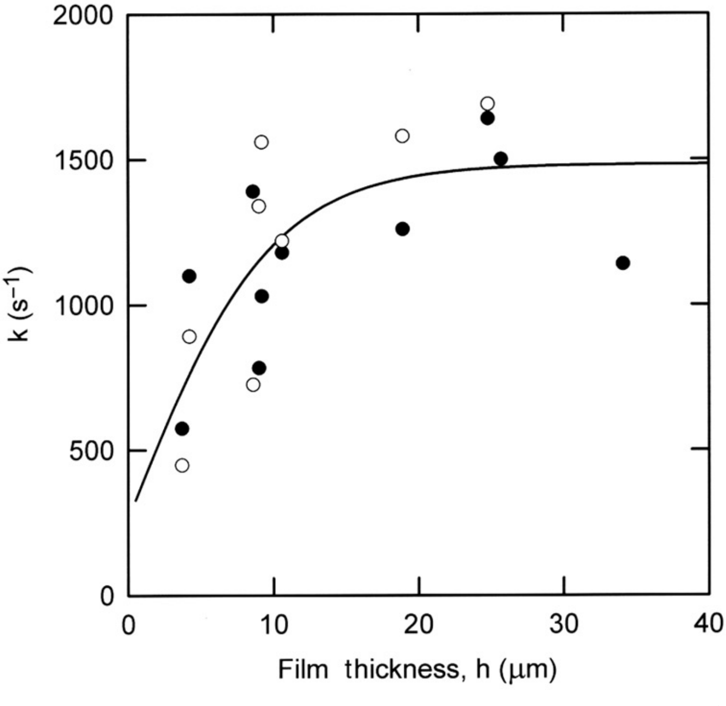

Figure 23. Plot of surface reaction rates corrected for external diffusion, k_g (s^{-1}) vs. substrate thickness, h (μm), for the reaction of $ClONO_2 + H_2O$ on H_2O ice substrates at 188 K. Filled circles are from $ClONO_2$ decay; open circles, HOCl growth. The analytical pore–diffusion model was used to correct the data for internal diffusion. The line through the data is a nonlinear regression fit to Equations (18)–(20). The best fit gives $\tau = 1.2 \pm 0.4$, $k_t = 265 \pm 31\ s^{-1}$, which corresponds to $\gamma_t = (2.3 \pm 0.3) \times 10^{-2}$.

vary and by using the values given in Table 6 for the other H_2O ice parameters. The best fit occurs for $k_t = 265 \pm 31\ s^{-1}$ and $\tau = 1.2 \pm 0.4$. The corresponding γ_t is $(2.3 \pm 0.3) \times 10^{-2}$.

5.2.2. *Application of layer model*

The individual data points were also corrected by using the layer model. In this case the HCP model variation was used since it closely approximates the H_2O ice substrate. Equations (36), (38), and (39) were used as well as the expression, Equation (19), for the effectiveness factor, η. A value of 1.2 was used for τ. An iterative procedure was used since the Thiele modulus, φ, depends on γ_t. An input value of γ_t was estimated and output values were compared to input values until they were equal to within 0.1%; usually less than 10 iterations were necessary. The resulting γ_ts are shown in columns 4 and 7 of Table 8; the overall average γ_t is $(1.5 \pm 0.5) \times 10^{-2}$. In this case, the layer–model result is about 50% lower than the analytical result.

5.2.3. *Summary of results for the reaction of $ClONO_2 + H_2O$ on H_2O ice*

The average value of γ after correction for the internal surface is about 0.02. The γ value is about a factor of 3 to 6 smaller than the values (~0.06 to 0.13) [see Table III of Ref. 58] based on the assumption that the geometric area of the flow reactor is the true ice surface area. Comparison with previous literature values based on the assumption that the available area for reaction is the geometric area of reactor is shown in Figure 24 [58–63].

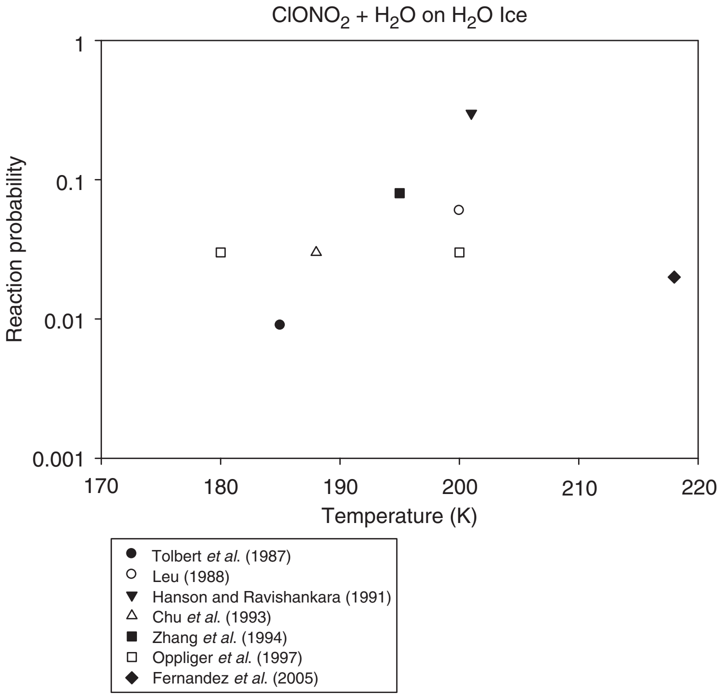

Figure 24. Comparison with literature values for the reaction $ClONO_2 + H_2O$ on ice surfaces.

Because these studies used a wide range of reactant concentrations and therefore the degree of surface deactivation by the build-up of reaction product HNO_3 on ice surfaces, the γ values are highly uncertain.

5.3. *Uptake of HCl on H_2O ice: Application of the HCP layer model*

The uptake or the amount of HCl adsorbed in H_2O ice was measured by using a flow–reactor interfaced with a quadrupole mass spectrometer described in Section 2.2 [22]. The HCl uptake in ice films at 188 and 193 K was determined at HCl partial pressures of 7×10^{-8} to 6×10^{-6} torr. Typical data at several ice thicknesses are shown in Figure 25. The total number of HCl molecules adsorbed was determined by integrating time dependent plots such as those shown in Figure 25. The uptake surface density can then be calculated using either the geometric area of the reactor surface or, if the ice substrate is porous, the total ice surface area. Total HCl uptake surface densities obtained from the data in Figure 25 are plotted vs. ice thickness in Figure 26. Another study shown in Figure 27 was performed at partial pressures of HCl near 5×10^{-7} torr at 196 K [27]. In Figures 26 and 27 the reactor geometric area has been used to calculate the uptake densities.

As shown in Figures 25–27, more HCl was taken up as the film thickness was increased. The uptake increased by about a factor of 10 from 1 to 50 μm. If the uptake occurs only on the surface of ice granules and solid-phase diffusion is very slow, this result

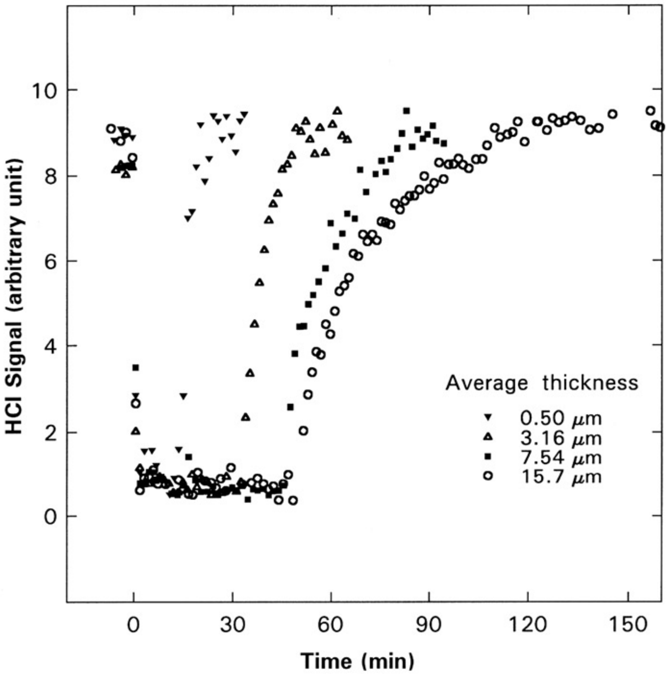

Figure 25. Time dependence plot of HCl uptake data at $p(\mathrm{HCl}) = 2.1 \times 10^{-7}$ torr and T = 188 K. The thickness of the ice film is varied from 0.5 to 15.7 μm.

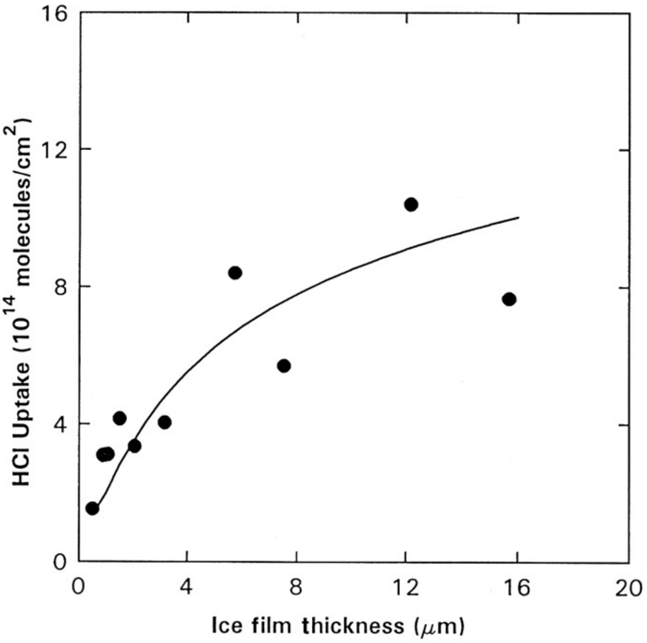

Figure 26. Plot of HCl uptake vs. ice film thickness at $p(\text{HCl}) = 2.1 \times 10^{-7}$ torr and $T = 188$ K. The line through the data is the best fit obtained by using the layer model and yields $\sim 2 \times 10^{13}$ molecule cm^{-2}.

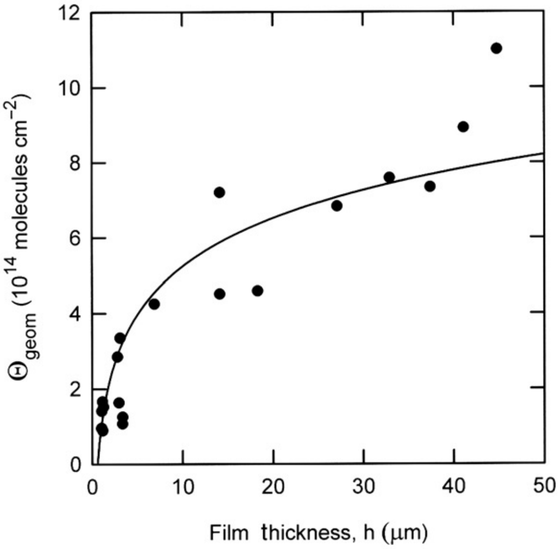

Figure 27. HCl uptake on H_2O ice vs. ice thickness. $P(\text{HCl}) = 5.0 \times 10^{-7}$ torr; $T = 196$ K. The HCP layer model was used to fit the data by nonlinear regression. The solid line is the best fit at $\Theta_t = (1.3 \pm 0.1) \times 10^{13}$ molecules cm^{-2}.

implies that the surface area available for HCl adsorption also increases by a factor of 10 over the same thickness range.

Since the uptake measurements are at steady state, the entire porous ice surface, external and internal, is involved. Under these conditions, the effectiveness factor, η, becomes unity and Equation (31) becomes

$$\Theta_{\mathrm{geom}} = \Theta_{\mathrm{t}}\rho_{\mathrm{b}}S_{\mathrm{g}}(h_{\mathrm{e}} + h_{\mathrm{i}}) \tag{41}$$

where Θ_{geom} and Θ_{t} have units of molecules cm^{-2} and are, respectively, the uptake density from the geometric area and the true uptake density, which accounts for the total ice surface area; $\rho_{\mathrm{b}}S_{\mathrm{g}}$ is the porous ice surface area per unit volume; and h_{e} and h_{i} are, respectively, the external and internal film thicknesses. Applying the layer model, Equation (41) becomes

$$\Theta_{\mathrm{geom}} = \Theta_{\mathrm{t}}\pi N_{\mathrm{L}} \quad \text{(for SCP)} \tag{42}$$

$$\Theta_{\mathrm{geom}} = \Theta_{\mathrm{t}}\pi 3^{-1/2}[2N_{\mathrm{L}} - 1 + (3/2)^{1/2}] \quad \text{(for HCP)} \tag{43}$$

We used the HCP layer model (Equation 43) to fit the uptake data for HCl on H_2O ice shown in Figure 27. Nonlinear regression was used with the layer distribution function: $N_{\mathrm{L}} = 2 + 9\log(\mathrm{h})$. The best fit plotted as the solid line in Figure 27 gives $\Theta_{\mathrm{t}} = (1.3 \pm 0.07) \times 10^{13}$ molecules cm^{-2}. Similarly, the best fit of the data shown in Figure 26 yields $\Theta_{\mathrm{t}} \sim 2 \times 10^{13}$ molecules cm^{-2} [22]. The results derived from the layer model yield a surface density smaller than that based on the geometric area of reactor.

HCl uptake is strongly dependent on temperature and partial pressure as shown in Figure 28. HCl uptake at 188 K is about a factor of 2 greater than that at 193 K.

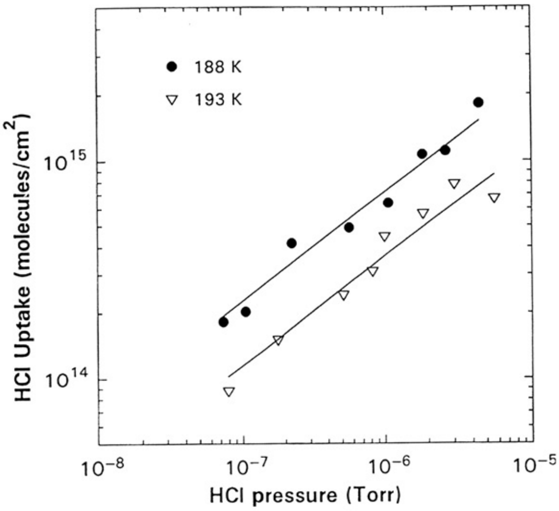

Figure 28. Plot of HCl uptake (use of geometric area of reactor) vs. partial pressure of HCl at 188 and 193 K. The solid lines in the figure are derived from a linear least-square fit to the data. The experimental conditions are $P_{\mathrm{total}} = 0.400$ torr, $v = 1730\,\mathrm{cm\,s^{-1}}$, $P_{\mathrm{ClONO2}} = 1.4 \times 10^{-7}$ torr, $P_{\mathrm{HCl}} = 5.1 \times 10^{-7}$ torr, $h = 12.5\,\mu$m, and $T = 188$ K. The HCl uptake at 188 K is slightly greater than that at 193 K.

Table 9. Studies of HCl uptake on vapor-deposited ice surfaces, based on the geometric area of reactor.

Investigator	Uptake, 10^{13} molecules cm^{-2}	T (K)	P(HCl), 10^{-7} torr	Ice thickness, μm	Method[a]
Marti *et al.*, 1991 [70]	10	200	1–10	1	KN
Abbatt *et al.*, 1992 [71]	100–300	201	10–40	5–40	FT
Hanson and Ravishankara, 1992 [72]	400–600	201	0.4–15	3–30	FT
Chu *et al.*, 1993 [22]	10–150	188, 193	0.7–40	1.4	FT
Chu *et al.*, 1993 [22]	10–100	188	2.1	0.5–16	FT
Foster *et al.*, 1997 [73]	40–2000	180–186	0.01–6	–	LITD
Leu *et al.*, 1997 [27]	10–110	196	5	1–45	FT
Barone *et al.*, 1999 [74]	350	202	500	0.05	KN
Lee *et al.*, 1999 [68]	30	201	20	–	FT
Huthwelker *et al.*, 2004 [75]	3–100	188–203	0.8–100	3–50	KN
Henson *et al.*, 2004 [76]	0.1–10	180–200	5–400	100	KN
McNeill *et al.*, 2007 [77]	2–20	196–213	0.5–25	–	FT

[a] KN: Knudsen cell, FT: Flow tube, LITD: Laser-induced thermal desorption.

Hence, comparison with literature values (see Table 9) must carefully take into account the temperature, HCl partial pressure and ice film thickness. The surface uptake appears to increase with ice thickness and HCl partial pressure, but, decrease with temperature.

In several previous investigations ice films were prepared by freezing liquid water in several laboratory investigations [64–71]. The results of these studies suggest that the HCl surface densities are about a factor of 3–10 greater than the data we derive from the layer model. The discrepancy might be resolved by: (1) better characterization of vapor deposited ice substrates, (2) refining the assumptions in the layer model of spherical ice granules with simple packing patterns, (3) measuring depth profiles during HCl uptake in ice substrates, and (4) better characterization of ice substrates obtained from freezing water. If surface HCl does not penetrate into the lower layers of ice substrates, the layer model may underestimate the surface density. Our recent BET adsorption measurements suggest that surface areas of borosilicate tubes and frozen H_2SO_4 are about a factor of 2 to 4 larger than the geometric area [21,78]. Moreover, careful examination of these surfaces by the ESEM shows a surface roughness consistent with the BET measurements [27].

Table 9 summarizes the comparison of our work with many other uptake measurements of HCl on vapor-deposited ice surfaces [69–77]. Because these investigators do not measure internal surface areas of ice substrates, for convenience, we consider the geometric area of reactor for HCl uptake only. The uptake amounts are highly uncertain owing to the dependence upon of ice thickness, temperature, and HCl pressures used in these studies [64].

5.4. *Reaction of $ClONO_2 + HCl$ on H_2O ice*

The reaction probability for this reaction was measured by observing the decay of $ClONO_2$ and the growth of Cl_2 [26,57,58]. Typical data are shown in Figure 29. The concentration of HCl used in the investigation was always greater than that of $ClONO_2$,

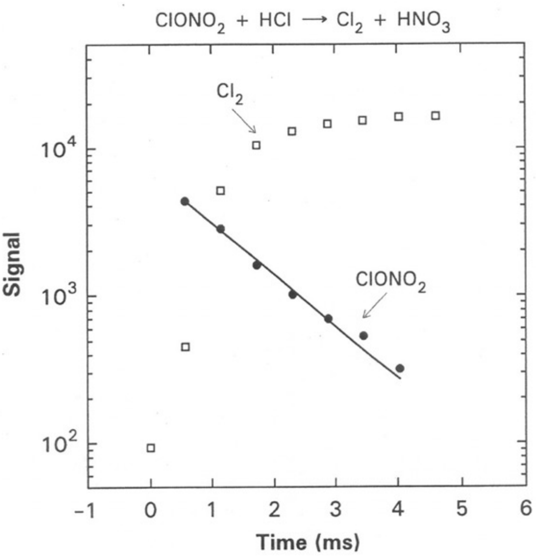

Figure 29. $ClONO_2$ decay and Cl_2 growth from the reaction of $ClONO_2 + HCl \rightarrow Cl_2 + HNO_3$ on H_2O ice surfaces.

thus a first–order rate constant can be calculated from the observed decay. We have varied P($ClONO_2$) in the range 6.5×10^{-8} to 9.7×10^{-7} torr and P(HCl) from 1.6×10^{-7} to 2.3×10^{-6} torr. The ice film thickness was about 10.4 ± 1.3 μm, and the temperature was 188 ± 0.5 K. These data are summarized in Figure 30. We obtained an average $\gamma_g = 0.26 \pm 0.19$ from the decay rate of $ClONO_2$ and $\gamma_g = 0.28 \pm 0.18$ from the growth of Cl_2. The overall average value of 24 experiments is 0.27 ± 0.19. The uncertainty represents one standard deviation. Using the model of surface reaction and pore diffusion, the true value is 0.10 ± 0.08. In addition, the Cl_2 yield based on the $ClONO_2$ reacted has been measured to be 1.2 ± 0.2.

Comparison with previous measurements is shown in Figure 31. Our results [25,28] are in good agreement with the literature values using the geometric area of the flow reactor or the Knudsen cell reactor as the available surface area for this reaction [25,58–63]. Within the error limits, the reaction probability appears to be temperature independent between 180 and 205 K.

5.5. *Reaction of $ClONO_2 + HCl$ on HNO_3–H_2O ice*

The reaction $ClONO_2 + HCl \rightarrow Cl_2 + HNO_3$ on HNO_3–H_2O ice was also investigated using the earlier version of the flow reactor [26,57]. Both $ClONO_2$ decay and Cl_2 growth were used to derive reaction probabilities and the results are shown in Figure 32. The reaction is uniformly fast for all substrate compositions in the range 40–60 wt%. The average γ value after correcting for the external diffusion is 0.27 ± 0.04 (1σ precision only). Using the analytical pore diffusion model, the average reaction probability is 0.1 ± 0.02 (1σ precision only) and is identical to that on H_2O ice. The larger γ value is consistent with

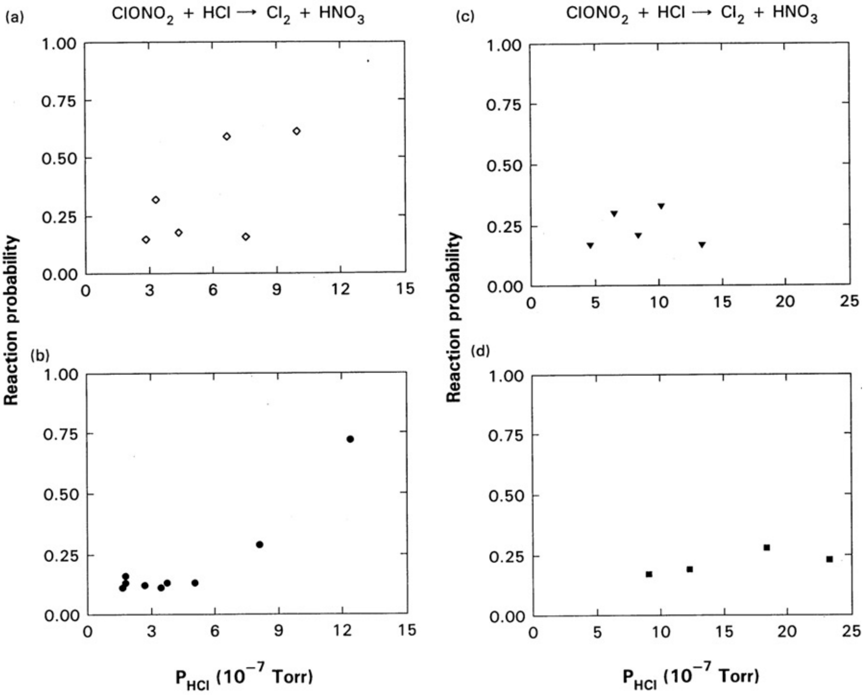

Figure 30. Summary of results for $ClONO_2 + HCl \rightarrow Cl_2 + HNO_3$ on H_2O ice. The data shown in this figure are average values obtained from $ClONO_2$ decay rates and from Cl_2 growth rates. Partial $ClONO_2$ pressures are (a) 6.6×10^{-8}, (b) 1.4×10^{-7}, (c) 3.1×10^{-7}, and (d) 9.7×10^{-7} torr.

literature values [79,81]. However, these workers did not consider pore diffusion through ice substrates as discussed in our work [26,57].

5.6. *Reaction of HOCl + HCl on H_2O ice*

The reaction probability for this reaction was measured by observing the decay of HOCl and growth of Cl_2 as a function of injector position [58]. The thickness of the ice film was $19.4 \pm 0.4\,\mu m$, and the temperature was $188 \pm 0.5\,K$. The results from these experiments using P(HOCl) in the range 1.3×10^{-7} to 1.8×10^{-6} torr and P(HCl) from 9×10^{-7} to 8×10^{-6} torr are summarized in Figure 33. The average $\gamma_g = 0.30 \pm 0.18$ from the decay rate of HOCl and $\gamma_g = 0.38 \pm 0.24$ from the growth of Cl_2. The overall average value of 41 experiments is 0.34 ± 0.20. The uncertainty represents one standard deviation. Using the model of surface reaction and pore diffusion, the true value is 0.13 ± 0.08. In addition, the Cl_2 yield based on the HOCl reacted has been measured to 0.80 ± 0.20.

Our results [58] are in good agreement with the literature values [62,79–81] using the geometric area of the flow reactor as the available surface area for this reaction as shown in Figure 34. Furthermore, the reaction probability appears to have a slightly negative temperature dependence in the range 185–205 K if we neglect the data by Chu and Chu [81] because of the use of higher concentrations of HOCl.

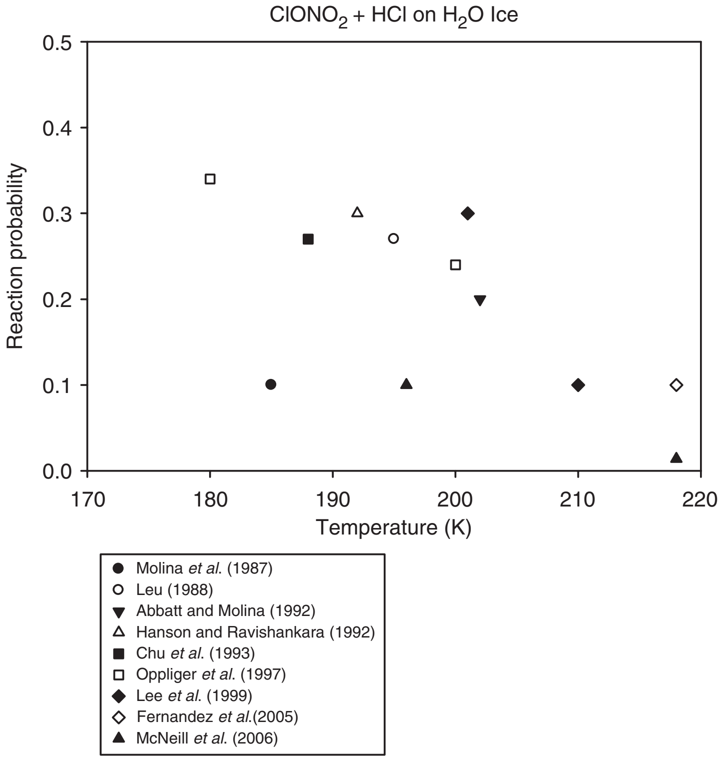

Figure 31. Comparison with literature values for the reaction $ClONO_2 + HCl \rightarrow Cl_2 + HNO_3$ on ice surfaces.

5.7. *Sticking coefficients of H_2O, HCl, and HNO_3 on H_2O ice*

We also measured the loss rates of H_2O, HCl, and HNO_3 on H_2O ice using another flow reactor [25]. The results are shown in Figure 35. The sticking coefficients of H_2O, HCl, and HNO_3 on H_2O ice based on the geometric area were determined to be 0.3 (+0.7, −0.1), 0.4 (+0.6, −0.2) and 0.3 (+0.7, −0.1), respectively at 200 K. Because of the diffusion limitation inside a cylindrical flow reactor, we have assigned much larger upper errors. The corrections due to the porous nature of ice substrates are estimated to be about a factor of 2 or 3.

Comparison with previously published data is shown in Figure 36 for HCl uptake on H_2O ice [60,65,66]. Uptake coefficients appear to show a negative temperature dependence, namely, greater values at lower temperatures. Similarly, we compare the uptake coefficient for HNO_3 on H_2O ice in Figure 37 [82–87]. The results are almost identical to that for HCl on ice.

5.8. *Application of theory to solid powder substrates*

Since solid powders, for example polycrystalline NaCl and many other inorganic salts, retain their morphology under laboratory investigations, both the pore diffusion model

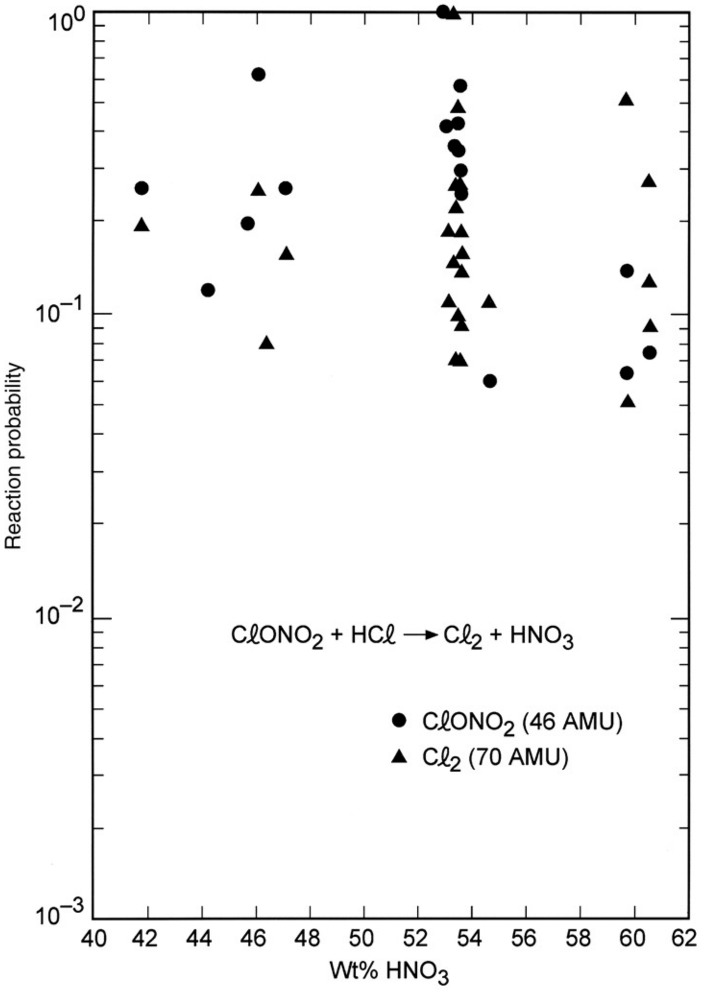

Figure 32. Summary of the data for the reaction of $ClONO_2 + HCl \rightarrow Cl_2 + HNO_3$ on HNO_3–H_2O ice surfaces. The reaction probabilities (corrected for the external diffusion only) are plotted versus weight percents of HNO_3 in the ice substrate. See text for the correction due to diffusion through porous medium.

and the layer model are suitable to derive uptake and reactivity coefficients with trace gases. Moreover, data from electron microscopy and adsorption isotherms can be compared with confidence. Using a modified flow reactor, we have studied several reactions: $ClONO_2 + NaCl \rightarrow NaNO_3 + Cl_2$ [88], $HNO_3 + NaCl \rightarrow NaNO_3 + HCl$ [89], $HNO_3 + NaBr \rightarrow NaNO_3 + HBr$ [90]. Because this review mainly presents our work on ice substrates, we will discuss only the reaction between HNO_3 and NaCl [89]. The result using NaCl powder and the layer model yields a γ value of (0.013 ± 0.004) which is significantly greater than the value of (0.0024 ± 0.0006) using smooth single crystal NaCl plates. The discrepancy may be due to the number of active sites per unit area, retention of surface water, and surface deactivation on the single crystals after the buildup of reaction

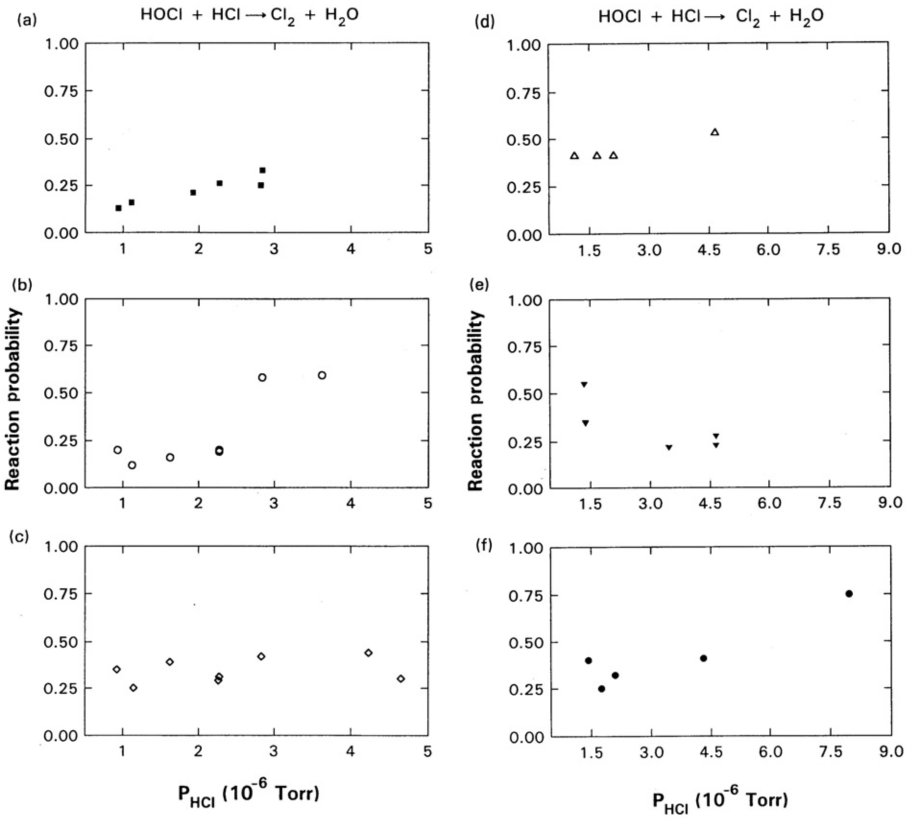

Figure 33. Summary of the data for the reaction of $HOCl + HCl \rightarrow Cl_2 + H_2O$ on H_2O ice surfaces. The data shown in this figure is the average value of the data obtained from the HOCl decay rates and from the Cl_2 growth rates. Partial HOCl pressures are (a) 1.3×10^{-7}, (b) 2.9×10^{-7}, (c) 5.6×10^{-7}, (d) 7.3×10^{-7}, (e) 1.2×10^{-6}, and (f) 1.8×10^{-6} torr.

product ($NaNO_3$). Similar issues are also evident in the investigation of water ice surfaces as noted in the previous sections.

The models we have developed are particularly suitable for applications using flow-tube reactors as well as low pressure Knudsen reactors. Several research groups leaded by M. J. Rossi [91], V. H. Grassian [92], Chu [93], Hanning-Lee [94] and H. Akimoto [95] have successfully investigated the interaction between trace gases and solid powders, for example, NaCl, NaBr, Al_2O_3, and sea salt. In studies such as these, it is necessary that precautions are taken to ensure: (1) that very low trace gas concentrations and short contact times are used to prevent the build-up of reaction products on the surface, (2) that the powders are out-gassed at high temperatures to eliminate residual surface adsorbed water, and (3) that the granule sizes and shapes of the sample are kept as uniform as possible. In addition, we note that weak or no dependence on substrate mass is usually observed at γs greater than 0.1 as predicted by the models. Detailed information has been given in both the IUPAC Gas Kinetic Data Evaluation [96] and the NASA Kinetics and Photochemical Data Evaluation [97].

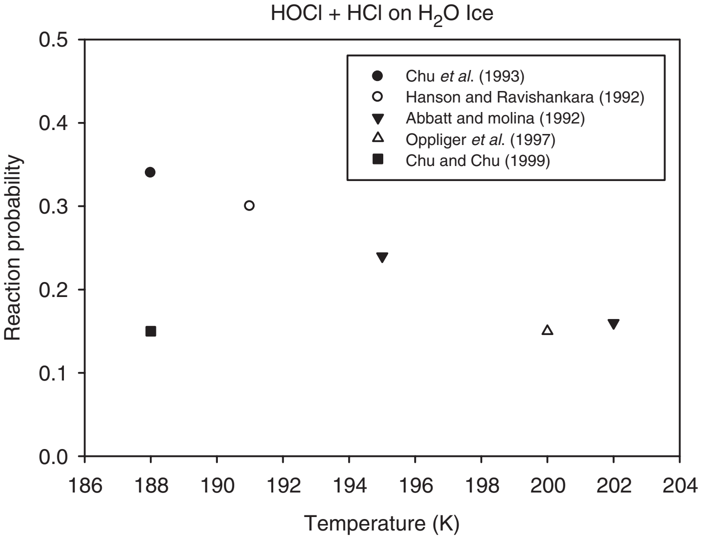

Figure 34. Comparison with literature values for the reaction $HOCl + HCl \rightarrow Cl_2 + H_2O$ on ice surfaces.

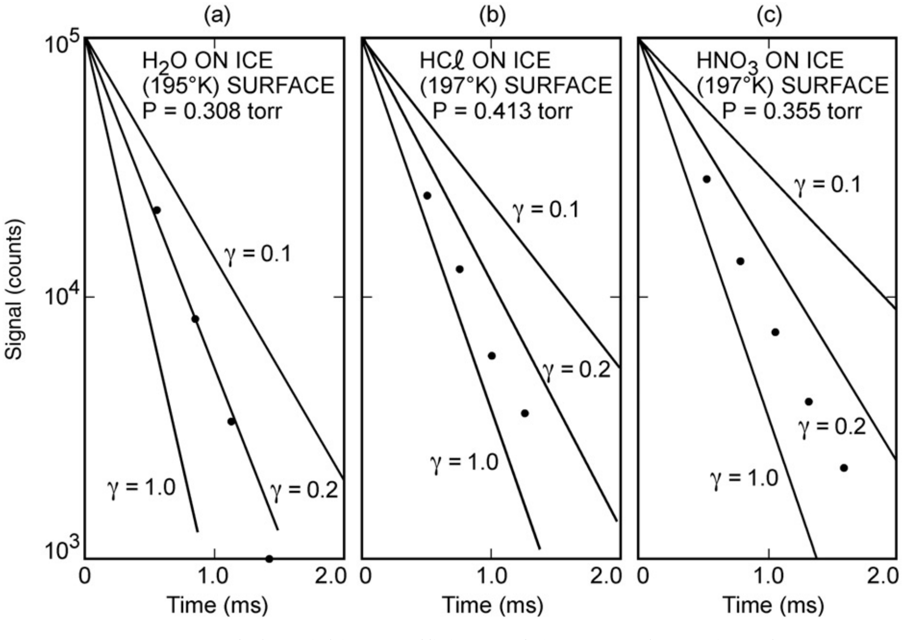

Figure 35. Measurements of the sticking coefficients of (a) H_2O, (b) HCl, and (c) HNO_3 on ice surfaces.

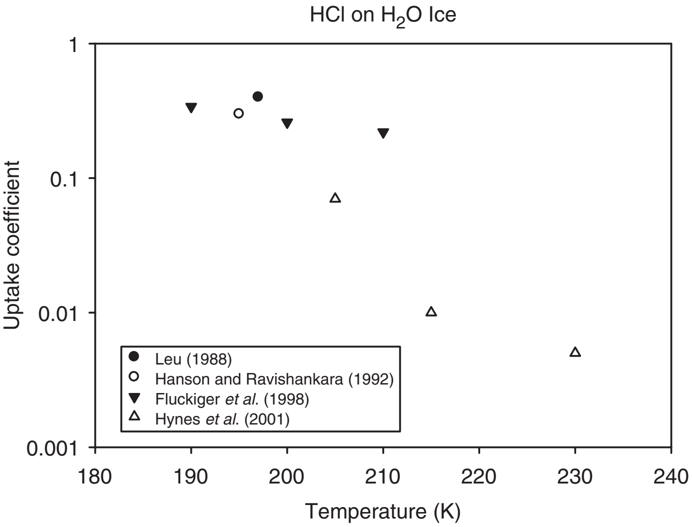

Figure 36. Comparison with literature values of HCl uptake coefficients on ice surfaces.

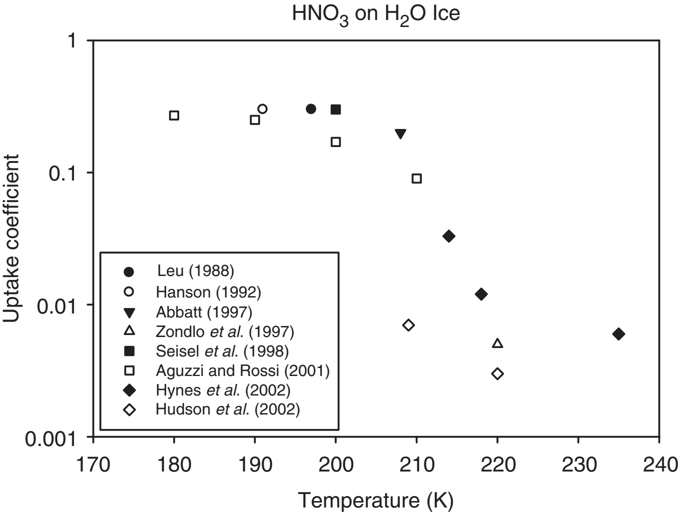

Figure 37. Comparison with literature values of HNO_3 uptake coefficients on ice surfaces.

6. Summary and future directions

In the past decade we have used several experimental apparatus, including flow-tube reactors, an electron-impact ionization mass spectrometer, a Fourier transform infrared spectrometer, BET adsorption cells, and a scanning environmental electron microscope to investigate the interaction between gas-phase species and ice. Numerous studies of atmospheric interest have been undertaken in our laboratory. In addition, we have developed theoretical models to elucidate the results of uptake and reactivity. In the following we will attempt to summarize our work presented in the preceding sections and to suggest future research directions in the study of vapor-deposited ices.

(1) Heterogeneous reactions on the surface of water ice and nitric acid ice play an important role in the springtime Antarctic stratosphere and lead to the severe ozone loss that has been evident since the early 1980s.
(2) Vapor-deposited ices have been identified to be porous as evidenced from electron microscopic observations; this conclusion is supported by BET adsorption isotherm measurements.
(3) The BET surface areas of ices may sometimes represent an upper limit to the areas available for reaction because some of the BET adsorption may be due to micropores and/or pore filling. It is important to confirm the BET results with optical or electron microscopic observations.
(4) The geometric surface areas of ices and crystals may represent a lower limit to the surface available for reaction because of microscopic roughness, cracks and/or dislocations. Here also it is important to confirm the surface condition experimentally.
(5) It has been suggested that the surfaces of the outer planets and their satellites in our solar system consist largely of very porous ices (~80–96% porosity). However, our observations of vapor-deposited ices by means of electron microscopy and adsorption isotherms seem to be less porous (~32%).
(6) Theoretical models using granule multi-layers and internal pore diffusion have been developed to account for porosities of vapor-deposited ices in the elucidation of uptake and reactivity data.
(7) Uptake of HCl in ice substrates has been measured in the temperature range 188–196 K. A surface coverage of $\sim 1.3 \times 10^{13}$ molecules cm^{-2} has been deduced from the granule layer model. The result is significantly greater than those based on the presumed 'smooth' surface of ice substrates.
(8) The heterogeneous reactions of $ClONO_2 + HCl \rightarrow Cl_2 + HNO_3$, $HOCl + HCl \rightarrow Cl_2 + H_2O$, and $ClONO_2 + H_2O \rightarrow HOCl + HNO_3$ on ices have been found to be very efficient in converting inactive chlorine to active forms. The pore diffusion model has been used to deduce true reaction probabilities for these reactions.
(9) Hydrogen affinity of water ice plays an important role in the sticking (or adsorption) of HCl and HNO_3 on ice surfaces.
(10) Because of diffusion limitations in flow reactors, both sticking coefficients and reaction probabilities on ices greater than ~0.3 cannot presently be measured by using this technique. It is very important to develop experimental techniques capable of accurately measuring larger γ values in the future. Under flow–tube conditions the rate can become diffusion limited but under atmospheric conditions it may not be and so it is still important to try and measure high γs independent of diffusion limitations.
(11) Theoretical models have been widely adopted in laboratory investigations of the reactivity of trace gases on porous powders using flow reactors and Knudsen cell reactors. However, caution must be used to ensure that minimal surface deactivation occurs by using very low reactant concentrations and short contact times.

(12) More theoretical work is needed to understand and account for surface deactivation by products and other contaminants.

(13) Modern experimental techniques, for example scanning electron microscopy with X-ray analysis, would be valuable to examine the surface condition of the ice substrates before and after uptake or reaction of these trace gases. Particularly, it is very important to find out the depth of the ice substrate available for these molecular processes.

Acknowledgements

This work was performed at the Jet Propulsion Laboratory, California Institute of Technology, under a contract with the National Aeronautics and Space Administration. We are grateful to our former colleagues, L. T. Chu, S. B. Moore, R. S. Timonen, T. L. Tso, R. H. Smith, C. S. Boxe, B. R. Bodsgard, and R. Zhang who have made important contributions to this work while they visited NASA–JPL.

Note

1. The product of $(1-\theta)\sigma$ is approximately unity for nitric acid ices; however, for water ice θ is about 0.3 and the product becomes 1.4. In the calculations described later in this paper, use of 1.4 for water ice instead of 1.0 affects the results by less than 16% so 1.0 is used in all the models and calculations.

References

[1] P. V. Hobbs, *Ice Physics* (Clarendon, Oxford, 1974).

[2] V. F. Petrenko and R. W. Whitworth, *Physics of Ice* (Oxford University Press, Oxford, 1999).

[3] T. R. Marrero and E. A. Mason, J. Phys. Chem. Ref. Data **1**, 3 (1972).

[4] J. C. Farman, B. G. Gardiner, and J. D. Shanklin, Nature **315**, 207 (1985).

[5] C. E. Kolb, D. R. Worsnop, M. S. Zahniser, P. Davidovits, D. R. Hanson, A. R. Ravishankara, L. F. Keyser, M.-T. Leu, L. R. Williams, M. J. Molina, and M. A. Tolbert, in *Progress and Problems in Atmospheric Chemistry*, edited by J. R. Barker (World Scientific, Singapore, 1995).

[6] M.-T. Leu, Int. Rev. Phys. Chem. **22**, 341 (2003).

[7] S. Solomon, R. R. Garcia, F. S. Rowland, and D. J. Wuebbles, Nature **321**, 755 (1986).

[8] L. T. Molina and M. J. Molina, J. Phys. Chem. **82**, 2410 (1987).

[9] Scientific Assessment of Ozone Depletion: 2006, WMO Global Ozone Research and Monitoring Project – Report No. 50.

[10] P. J. Crutzen and F. Arnold, Nature **324**, 651 (1986).

[11] O. B. Toon, P. Hamill, R. P. Turco, and J. Pinto, Geophys. Res. Lett. **13**, 1284 (1986).

[12] R. H. Brown, R. N. Clark, B. J. Buratti, D. P. Cruikshank, J. W. Barnes, R. M. E. Mastrapa, J. Bauer, S. Newman, T. Momary, K. H. Baines, G. Bellucci, F. Capaccioni, P. Cerroni, M. Combes, A. Coradini, P. Drossart, V. Formisano, R. Jaumann, Y. Langevin, D. L. Matson, T. B. McCord, R. M. Nelson, P. D. Nicholson, B. Sicardy, and C. Sotin, Science **311**, 1425 (2006).

[13] A. Coustenis, A. Negrão, A. Salama, B. Schulz, E. Lellouch, P. Rannou, P. Drossart, T. Encrenaz, B. Schmitt, V. Boudon, and A. Nikitin, Icarus **180**, 176 (2006).

[14] G. Hansen, *et al.*, AGU Fall Meeting, San Francisco, CA, USA (2005).

[15] G. Hansen and T. B. McCord, J. Geophys. Res. – Planets, **109**, E01012 (2004).

[16] B. Hapke, J. Geophys. Res. **86**, 3055 and 3093 (1981).

[17] B. J. Buratti, Icarus **92**, 312 (1991).

[18] B. J. Buratti, J. Geophys. Res. – Planets **100**, 19061 (1995).

[19] D. L. Domingue, B. W. Hapke, G. W. Lockwood, and D. T. Thompson, Icarus **90**, 30 (1991).

[20] D. Domingue and A. Verbiscer, Icarus **128**, 49 (1997).

[21] C. S. Boxe, B. R. Bodsgard, W. Smythe, and M.-T. Leu, J. Colloid Interface Sci. **309**, 412 (2007).

[22] L. T. Chu, M.-T. Leu, and L. F. Keyser, J. Phys. Chem. **97**, 7779 (1993).

[23] R. L. Brown, J. Res. Natl. Bur. Stand. (US) **83**, 1 (1979).

[24] F. Kaufman, Prog. React. Kinet. **1**, 1 (1961).

[25] M.-T. Leu, Geophys. Res. Lett. **15**, 17 (1988).

[26] S. B. Moore, L. F. Keyser, M. T. Leu, *et al.*, Nature **345**, 333 (1990).

[27] M.-T. Leu, R. S. Timonen, and L. F. Keyser, J. Phys. Chem. A **101**, 278 (1997).

[28] L. F. Keyser and M.-T. Leu, Microscopy Res. Technique **25**, 434 (1993).

[29] L. F. Keyser and M.-T. Leu, J. Colloid Interface Sci. **155**, 137 (1993).

[30] S. J. Gregg and K. S. W. Sing, *Adsorption, Surface Area and Porosity* (Academic Press, New York, 1982).

[31] A. J. Rosenberg, J. Am. Chem. Soc. **78**, 2929 (1956).

[32] E. Mayer and R. Pletzer, Nature **319**, 298 (1986); J. de Phys. **48 C1**, 581 (1987).

[33] A. Bar-Nun, J. Dror, E. Kochavi, and D. Laufer, Phys. Rev. B **35**, 2427 (1987).

[34] A. W. Adamson, L. M. Dormant, and M. Orem, J. Colloid Interface Sci. **25**, 206 (1967).

[35] B. Schmitt, J. Ocampo, and J. Klinger, J. de Phys. **48 C1**, 519 (1987).

[36] B. J. Murray and J. M. C. Plane, Phys. Chem. Chem. Phys. **5**, 4129 (2003).

[37] C. Manca, C. Martin, and P. Roybin, Chem. Phys. Lett. **364**, 220 (2002).

[38] C. Pierce, J. Phys. Chem. **57**, 149 (1953).

[39] I. Taesler, R. G. Delaplane, and I. Olovsson, Acta Crystallorg. Sect B **31**, 1489 (1975).

[40] R. H. Smith, M.-T. Leu, and L. F. Keyser, J. Phys. Chem. **95**, 5924 (1991).

[41] T.-L. Tso and M.-T. Leu, Analytical Sci. **12**, 615 (1996).

[42] G. Ritzhaupt and T. P. Devlin, J. Phys. Chem. **95**, 90 (1991).

[43] B. G. Koehler, A. M. Middlebrook, and M. A. Tolbert, J. Geophys. Res. **97**, 8065 (1992).

[44] L. F. Keyser, S. B. Moore, and M.-T. Leu, J. Phys. Chem. **95**, 5496 (1991).

[45] L. F. Keyser, M.-T. Leu, and S. B. Moore, J. Phys. Chem. **97**, 2800 (1993).

[46] R. E. Walker, Phys. Fluids **4**, 1211 (1961).

[47] C. J. Howard, J. Phys. Chem. **83**, 3 (1979).

[48] F. Kaufman, J. Phys. Chem. **88**, 4909 (1984).

[49] L. F. Keyser, J. Phys. Chem. **88**, 4750 (1984).

[50] E. W. Thiele, Ind. Eng. Chem. **31**, 916 (1939).

[51] A. Wheeler, Adv. Catal. **3**, 249 (1951).

[52] A. Wheeler, in *Catalysis, Fundamental Principles*, edited by P. H. Emmett (Reinhold, New York, 1955), Vol. 2, pp. 105–165.

[53] A. Clark, *The Theory of Adsorption and Catalysis* (Academic Press, New York, 1970).

[54] J. J. Carberry, *Chemical and Catalytic Reaction Engineering* (McGraw–Hill, New York, 1976).

[55] R. Aris, *The Mathematical Theory of Diffusion and Reaction in Permeable Catalysis* (Clarendon Press, Oxford, 1971), Vol. 1.

[56] J. M. Zielinski and E. E. Peterson, AlChE J. **33**, 1993 (1987).

[57] M.-T. Leu, S. B. Moore, and L. F. Keyser, J. Phys. Chem. **95**, 7763 (1991).

[58] L. T. Chu, M.-T. Leu, and L. F. Keyser, J. Phys. Chem. **97**, 12798 (1993).

[59] M. A. Tolbert, M. J. Rossi, R. Malhotra, and D. M. Golden, Science **238**, 1903 (1987).

[60] D. R. Hanson and A. R. Ravishankara, J. Geophy. Res. **96**, 5081 (1991).

[61] R. Zhang, J. T. Jayne, and M. J. Molina, J. Phys. Chem. **98**, 867 (1994).

[62] R. Oppliger, A. Allanic, and M. J. Rossi, J. Phys. Chem. A **101**, 1903 (1997).

[63] M. A. Fernandez, R. G. Hynes, and R. A. Cox, J. Phys. Chem. A **109**, 9986 (2005).

[64] T. Huthwelker, M. Ammann, and T. Peter, Chem. Rev. **106**, 1375 (2006).

[65] B. Fluckiger, A. Thielmann, L. Gutzwiller, and M. J. Rossi, Ber. Bunsenges. Phys. Chem. **102**, 915 (1998).

[66] R. G. Hynes, J. Mossinger, and R. A. Cox, Geophys. Res. Lett. **28**, 2827 (2001).

[67] R. G. Hynes, M. A. Fernandez, and R. A. Cox, J. Geophys. Res. **107**, 4797 (2002).

[68] S.-H. Lee, D. C. Leard, R. Zhang, L. T. Molina, and M. J. Molina, Chem. Phys. Lett. **315**, 7 (1999).

[69] V. F. McNeill, T. Loerting, F. M. Geiger, B. L. Trout, L. T. Molina, and M. J. Molina, Proc. Nat. Acad. Sci. (USA) **103**, 9422 (2006).

[70] J. Marti, K. Mauersberger, and D. Hanson, Geophys. Res. Lett. **18**, 1861 (1991).

[71] J. P. D. Abbatt, K. D. Beyer, A. F. Fucaloro, J. R. McMahon, P. J. Wooldridge, R. Zhang, and M. J. Molina, J. Geophys. Res. **97**, 15918 (1992).

[72] D. R. Hanson and A. R. Ravishankara, J. Geophy. Res. **96**, 5081 (1991).

[73] K. L. Foster, M. A. Tolbert, and S. M. George, J. Phys. Chem. **101**, 4979 (1997).

[74] S. Barone, M. A. Zondlo, and M. A. Tolbert, J. Phys. Chem. **103**, 9717 (1999).

[75] T. Huthwelker, M. E. Malmstrom, F. Helleis, G. K. Moortgat, and T. Peter, J. Phys. Chem. A **108**, 6302 (2004).

[76] B. F. Henson, K. R. Wilson, J. M. Robinson, C. A. noble, H. L. Casson, and D. R. Worsnop, J. Chem. Phys. **121**, 8486 (2004).

[77] V. F. McNeill, F. M. Geiger, T. Loerting, B. L. Trout, L. T. Molina, and M. J. Molina, J. Phys. Chem. A **111**, 6274 (2007).

[78] R. Zhang, M. T. Leu, and L. F. Keyser, J. Geophys. Res. **100**, 18845 (1995).

[79] D. R. Hanson and A. R. Ravishankara, J. Phys. Chem. **96**, 2682 (1992).

[80] J. P. D. Abbatt and M. J. Molina, J. Phys. Chem. **96**, 7674 (1992).

[81] L. Chu and L. T. Chu, J. Phys. Chem A **103**, 691 (1999).

[82] D. R. Hanson, Geophys. Res. Lett. **19**, 2063 (1992).

[83] J. P. D. Abbatt, Geophys. Res. Lett. **24**, 1479 (1997).

[84] M. A. Zondlo, S. B. Barone, and M. A. Tolbert, Geophys. Res. Lett. **24**, 1391 (1997).

[85] S. Seisel, B. Fluckiger, and M. J. Rossi, Ber. Bunsenges. Phys. Chem. A **102**, 811 (1998).

[86] A. Agguzzi and M. J. Rossi, Phys. Chem. Chem. Phys. **3**, 3707 (2001).

[87] P. K. Hudson, J. E. Shilling, M. A. Tolbert, and O. B. Toon, J. Phys. Chem A **106**, 9874 (2002).

[88] R. Timonen, L. T. Chu, M.-T. Leu, and L. F. Keyser, J. Phys. Chem. **98**, 9509 (1994).

[89] M.-T. Leu, R. S. Timonen, L. F. Keyser, and Y. L. Yung, J. Phys. Chem. **99**, 13203 (1995).

[90] M.-T. Leu, L. F. Keyser, and R. S. Timonen, J. Phys. Chem. B **101**, 6259 (1997).

[91] R. Oppliger, A. Allanic, and M. J. Rossi, J. Phys. Chem. A **101**, 1903 (1997).

[92] T. M. Miller and V. H. Grassian, Geophys. Res. Lett. **25**, 3835 (1998).

[93] L. T. Chu, G. Diao, and L. Chu, J. Phys. Chem. B **106**, 5679 (2002).

[94] M. A. Hanning-Lee, B. B. Brady, L. R. Martin, and J. A. Syage, Geophys. Res. Lett. **23**, 1961 (1996).

[95] M. Mochida, J. Hirokawa, Y. Kajii, and H. Akimoto, Geophys. Res. Lett. **27**, 2629 (2000).

[96] IUPAC Subcommittee on Gas Kinetic Data Evaluation (2007).

[97] NASA Kinetics and Photochemical Data Evaluation (2006).